

Precipitation and growth of barite within hydrothermal vent deposits from the Endeavour Segment, Juan de Fuca Ridge

John William Jamieson^{1,2,*} (jjamieson@geomar.de)
Mark D. Hannington^{1,2} (mhannington@geomar.de)
Margaret K. Tivey³ (mktivey@whoi.edu)
Thor Hansteen¹ (thansteen@geomar.de)
Nicole M-B. Williamson² (nmb.williamson@gmail.com)
Margaret Stewart⁴ (meg.engelbert@gmail.com)
Jan Fietzke¹ (jfietzke@geomar.de)
David Butterfield⁵ (david.a.butterfield@noaa.gov)
Matthias Frische¹ (mfrische@geomar.de)
Leigh Allen² (Leigh.alle@gmail.com)
Brian Cousens⁴ (brian.cousens@carleton.ca)
Julia Langer¹ (j.-langer@outlook.com)

¹GEOMAR – Helmholtz Centre for Ocean Research Kiel
Wischhofstr. 1-3, 24148 Kiel, Germany

²University of Ottawa
FSS Hall, 120 University, Ottawa, ON, K1N 6N5, Canada

³Woods Hole Oceanographic Institution
266 Woods Hole Road, Woods Hole, MA 02543-1050 USA

⁴Carleton University
1125 Colonel By Drive, Ottawa, ON, K1S 5B6, Canada

⁵University of Washington and NOAA/PMEL
7600 Sand Point Way NE, Seattle, WA, 98115, USA

*Corresponding Author: jjamieson@geomar.de

Abstract

Hydrothermal vent deposits form on the seafloor as a result of cooling and mixing of hot hydrothermal fluids with cold seawater. Amongst the major sulfide and sulfate minerals that are preserved at vent sites, barite (BaSO_4) is unique because it requires the direct mixing of Ba-rich hydrothermal fluid with sulfate-rich seawater in order for precipitation to occur. Because of its extremely low solubility, barite crystals preserve geochemical fingerprints associated with

conditions of formation. Here, we present data from petrographic and geochemical analyses of hydrothermal barite from the Endeavour Segment of the Juan de Fuca Ridge, northeast Pacific Ocean, in order to determine the physical and chemical conditions under which barite precipitates within seafloor hydrothermal vent systems. Petrographic analyses of 22 barite-rich samples show a range of barite crystal morphologies: dendritic and acicular barite forms near the exterior vent walls, whereas larger bladed and tabular crystals occur within the interior of chimneys. A two component mixing model based on Sr concentrations and $^{87}\text{Sr}/^{86}\text{Sr}$ of both seawater and hydrothermal fluid, combined with $^{87}\text{Sr}/^{86}\text{Sr}$ data from whole rock and laser-ablation ICP-MS analyses of barite crystals indicate that barite precipitates from mixtures containing as low as 17% and as high as 88% hydrothermal fluid component, relative to seawater. Geochemical modelling of the relationship between aqueous species concentrations and degree of fluid mixing indicates that Ba^{2+} availability is the dominant control on mineral saturation. Observations combined with model results support that dendritic barite forms from fluids of less than 40% hydrothermal component and with a saturation index greater than ~ 0.6 , whereas more euhedral crystals form at lower levels of supersaturation associated with greater contributions of hydrothermal fluid. Fluid inclusions within barite indicate formation temperatures of between ~ 120 and 240°C during barite crystallization. The comparison of fluid inclusion formation temperatures to modelled mixing temperatures indicates that conductive cooling of the vent fluid accounts for $60 - 120^\circ\text{C}$ reduction in fluid temperature. Strontium zonation within individual barite crystals records fluctuations in the amount of conductive cooling within chimney walls that may result from cyclical oscillations in hydrothermal fluid flux. Barite chemistry and morphology can be used as a reliable indicator for past conditions of mineralization within both extinct seafloor hydrothermal deposits and ancient land-based volcanogenic massive sulfide deposits.

Introduction

Heat from shallow magmatic activity drives the circulation of seawater through oceanic crust along volcanically-active mid-ocean ridges, arcs, and back-arc basins (Baker et al., 1995; Hannington et al., 2005). As fluids circulate, they are heated, and react with the surrounding rock, resulting in leaching and transport of dissolved chemical constituents from the underlying substrate to the seafloor. Hydrothermal chimneys and mounds form on the seafloor at sites where the high temperature, focused hydrothermal fluid discharges, and where mineral precipitation is driven by the mixing of the hot vent fluid with local cold seawater (Hannington et al., 1995; Von Damm, 1990).

The composition of the substrate is a major control on both vent fluid composition and the mineralogy of the hydrothermal deposits that form on the seafloor (e.g., Von Damm, 1990).

The primary minerals that typically make up vent edifices are sulfides such as pyrite, sphalerite, chalcopyrite, pyrrhotite, sulfates such as barite and anhydrite, and amorphous silica. These minerals precipitate either from dissolved constituents within the hydrothermal fluids (e.g., pyrite precipitated from dissolved Fe^{2+} and H_2S or HS^-), from dissolved constituents within locally heated seawater (e.g., anhydrite precipitated from dissolved Ca^{2+} and SO_4^{2-}), or from dissolved constituents within both fluids (e.g., barite and anhydrite precipitated from Ba^{2+} and Ca^{2+} , respectively, in hydrothermal fluid that has mixed with SO_4^{2-} -rich seawater) (Hannington et al., 2005; Humphris and Bach, 2005; Tivey et al., 1999; Von Damm, 1990). Mineral precipitation is driven mainly by the changes in temperature, pH, $f\text{O}_2$, and concentration of dissolved ions that accompany the mixing of hot hydrothermal fluid and cold seawater, although fluid temperature can also be affected by conductive cooling and heating (Hannington et al., 1995; Ruiz-Agudo et al., 2015; Tivey, 1995; Tivey and McDuff, 1990; Tivey et al., 1999). The occurrence of specific minerals or mineral assemblages within a chimney thus largely reflects the physicochemical properties of the local fluid at the time of precipitation. High-temperature minerals (minerals that precipitate at temperatures above $\sim 300^\circ\text{C}$, such as chalcopyrite, pyrrhotite, wurtzite) precipitate primarily along inner fluid conduits, where there is limited infiltration of cold seawater (Hannington et al., 1995). The porous outer chimney walls typically contain a lower-temperature ($< \sim 300^\circ\text{C}$) suite of minerals (e.g., sphalerite, barite, and amorphous silica) that precipitate as a result of a higher degree of mixing with seawater, and/or conductive cooling of the hydrothermal fluid (Hannington et al., 1995; Tivey et al., 1999).

Barite and other low-temperature minerals dominate the early and late growth stages of a hydrothermal chimney that are characterized by lower hydrothermal fluxes and fluid temperatures (Hannington et al., 1995; Tivey et al., 1990). However, precipitation of these low-temperature minerals will still occur within chimneys formed from high-temperature venting, often in the exterior walls of a chimney where extensive mixing with seawater occurs (Hannington et al., 1991; Hannington and Scott, 1988). Barite is especially important as a key structural component to hydrothermal edifices on the seafloor, and its occurrence and abundance can affect hydrothermal deposit morphology, the style of venting and chimney growth, and the retention of metals within a deposit (Hannington et al., 1995; Tivey and Delaney, 1986). Precipitation of barite occurs when the product of the concentrations of Ba^{2+} (from the hydrothermal fluid) and SO_4^{2-} (from seawater) exceed the solubility constant of the mixed fluid (Blount, 1977). End-member concentrations of Ba in hydrothermal fluids from Main Endeavour Field have been measured at concentrations of up to $31 \mu\text{mol/kg}$ (Seyfried et al., 2003), indicating significant enrichment of Ba relative to ambient seawater ($0.1 \mu\text{mol/kg}$) resulting from leaching of Ba during hydrothermal alteration of basalt (Chan et al., 1976; Kim and McMurtry, 1991). Modern seawater contains $\sim 28 \text{ mmol/kg}$ of dissolved sulfate, whereas

sulfate concentrations in endmember hydrothermal fluids are generally near zero as a result of precipitation of anhydrite within the crust and the thermo-chemical reduction of remaining sulfate during high-temperature reactions with basalt (Halevy et al., 2012; Seyfried et al., 2003). In contrast to anhydrite, which is unstable and will dissolve at ambient seafloor temperatures, barite has extremely low solubility in seawater and behaves as a closed system under typical oxic seafloor conditions, and is not prone to diagenetic alteration (Averyt and Paytan, 2003, and references therein; Widanagamage et al., 2014). Barite can thus preserve geochemical and morphological features associated with initial conditions of crystallization long after hydrothermal venting has ceased, and the occurrence, and crystallographic and geochemical properties of barite can provide insights into fluid mixing and the physicochemical conditions that drive mineral precipitation within the walls of hydrothermal chimneys. Barite is also the primary host in hydrothermal deposits for Ra, a radiogenic element that also has a similar ionic charge and radius to Ba. The closed system behavior of barite allows for the decay of ^{226}Ra (half-life of 1,600 years) within the crystals to be used to determine absolute ages of chimneys (de Ronde et al., 2005; Ditchburn et al., 2004; Ditchburn et al., 2012; Jamieson et al., 2013a). Strontium is an abundant dissolved cation in both seawater and hydrothermal fluids, with seawater and Endeavour hydrothermal concentrations of $\sim 87 \mu\text{mol/kg}$ and $\sim 135 \mu\text{mol/kg}$, respectively (Butterfield et al., 1994; Seyfried et al., 2003; Turekian, 1968). With a similar ionic charge and radius to Ba, Sr is a common trace substitution in barite. At the same time, both seawater and hydrothermal fluid at Endeavour have very different Sr-isotope ($^{87}\text{Sr}/^{86}\text{Sr}$) ratios. These ratios can be compared to the ratios measured in barite crystals to determine the relative proportion of seawater and hydrothermal fluid that make up the fluid mixture from which barite precipitated. A similar approach has been used to investigate the precipitation of anhydrite within the main active mound at the TAG hydrothermal field on the Mid-Atlantic Ridge (Mills et al., 1998; Teagle et al., 1998) and the 21-Degrees North site on the East Pacific Rise (Albarede et al., 1981). However, there are few reports of similar studies for hydrothermal barite (Kusakabe et al., 1990).

In this study, we present data on the morphology, trace element distribution, Sr-isotope composition and fluid inclusion analysis of barite collected from active and inactive hydrothermal chimneys on the Endeavour Segment of the Juan de Fuca Ridge. The integrated analysis of these multiple datasets provides constraints on the physical and chemical controls associated with fluid mixing for barite precipitation within hydrothermal chimney walls. Results of geochemical modeling are used to link the qualitative petrographic observations of barite occurrence within the vent chimneys to the quantitative constraints on fluid mixing and the physicochemical conditions of barite precipitation. This information can be used to infer the formation temperatures and fluid chemistry of inactive chimneys, provide insights into the role

of fluid mixing within chimneys for the precipitation of other chimney-forming minerals, and evaluate the locations favourable for microbial habitat within chimneys.

Geological Setting

The Endeavour Segment is a 90 km-long section of the Juan de Fuca mid-ocean ridge, which is spreading at an average full-spreading rate of ~6 cm/yr (Fig. 1) (Goldstein et al., 1991; Riddihough, 1984). The segment, shown in red in the inset of Figure 1, is bound to the south by the Cobb Offset and the Cobb overlapping spreading center (OSC) and to the north by the Endeavour Offset and the Endeavour OSC. The Cobb Offset represents a major geochemical division in the Juan de Fuca Ridge, with normal mid-ocean ridge basalt (N-MORB) dominating the oceanic crust south of the offset and enriched-MORB (E-MORB) dominating oceanic crust north of the offset (Karsten et al., 1990). The occurrence of E-MORB at Endeavour has been attributed to a heterogeneous mantle source of both enriched and depleted upper mantle with the enriched component of the mantle source exhibiting enhanced melting relative to the depleted mantle source (Cousens, 2010).

The Endeavour Segment ranges in depth from 2050 meters below sea level (mbsl) at a central bathymetric high to >2700 mbsl towards the south end of the segment (Fig. 1) (Delaney et al., 1992). Active hydrothermal venting is focused within a 15 km-long central axial valley that bisects the central volcanic high (Kelley et al., 2012). Within the axial valley are five major hydrothermal vent fields (Sasquatch, Salty Dawg, High Rise, Main Endeavour Field, Mothra), with several smaller vent fields and diffusely venting areas, making the Endeavour Segment one of the most active hydrothermal areas on the mid-ocean ridge system (Fig. 1) (Kelley et al., 2012). Numerous inactive or extinct sulfide edifices occur on the axial valley floor outside of the active vent fields (Clague et al., 2008; Jamieson et al., 2014). Hydrothermal activity has been ongoing within the axial valley for at least the past ~3,000 years (Jamieson et al., 2013a).

The sulfide edifices at Endeavour are typically steep-sided, often reaching heights of greater than 20 metres above the seafloor, with fluid venting temperatures that range from <10°C up to ~375°C (Butterfield et al., 1994; Delaney et al., 1992; Glickson et al., 2006; Kelley et al., 2012; Robigou et al., 1993). The edifices are rich in barite relative to typical mid-ocean ridge deposits. The high abundance of barite has been linked to the high Ba content of the underlying E-MORB crust (Karsten et al., 1990; Tivey et al., 1999) and/or the presence of buried sediments that have modified the chemistry of the hydrothermal fluids prior to venting (Butterfield et al., 1994; Lilley et al., 1993; Proskurowski et al., 2004; Yao et al., 2009; You et al., 1994).

Vent fluid chemistry within the Main Endeavour Field has been shown to be remarkably stable from year to year (Butterfield et al., 1994). However, significant changes in fluid composition over short periods have been linked to local seismic events (Seyfried et al., 2003). Factors such

as low chlorinity relative to seawater, and short-lived venting of high-temperature, volatile-rich fluids suggest that subsurface phase separation is an ongoing process (Butterfield et al., 1994; Kelley et al., 2012; Larson et al., 2009).

Analytical Methods

Barite-rich samples for this study were collected from active and inactive hydrothermal structures using remotely-operated vehicles (ROVs) and occupied submersible during several research cruises to the Endeavour Segment between 1984 and 2011 (Delaney et al., 1992; Glickson et al., 2006; Glickson et al., 2007; Jamieson et al., 2013a; Kelley et al., 2012; Kelley et al., 2001; Kristall et al., 2006; Robigou et al., 1993; Tivey et al., 1999). Samples are generally fist-sized, and therefore their contained mineralogy and bulk chemistry may not reflect that of the entire vent from which they were sampled. Thin sections and doubly-polished thick sections (80 μm) were prepared for petrographic and fluid inclusion analysis, respectively, by first impregnating the samples in epoxy due to their fragile nature, and then cutting and polishing each sample. Thin sections were examined using both reflected and transmitted light modes with an Olympus BX 51 polarizing microscope with an attached Olympus DP71 digital camera.

Two samples – ALV2464-R4 and ALV2467-R2 – were selected for detailed analysis of barite growth due to their large (>0.5 mm), euhedral zoned tabular barite crystals (Fig. 2). Sample ALV2464-R4 is barite-rich and sulfur-poor, and was collected from the side of an old, Mn-coated 1.5 m tall, 1 m wide extinct spire within the High Rise vent field. ALV2467-R2 was collected from a tall, thin extinct spire north of the Main Endeavour field.

Geochemistry

Concentrations of Ba, Ca and Sr within bulk samples were determined at ActLabs, in Ontario, Canada, using a combination of fusion followed by multi-acid dissolution and inductively coupled mass spectrometry, instrumental neutron activation analysis (for Ba), and inductively-coupled plasma emission spectroscopy (for Ca and Sr). The reporting uncertainties are $<10\%$ over the range of measured concentrations.

Electron microprobe analysis

Concentrations of Sr, Ba, Ca and SO_4 within individual barite crystals were determined by electron microprobe analysis (EMPA). Barites from seven carbon-coated thin-sections were analyzed using an automated 4-spectrometer Cameca Camebax MBX electron microprobe at Carleton University, using both energy-dispersive and wavelength-dispersive analytical modes, with an accelerating voltage of 15 keV and a 20 nA beam current. Samples were selected in order to maximize the variability in sample bulk Sr/Ba and barite crystal morphology. Analyses for Fe, Cl, Cu and Zn returned concentrations below analytical detection limits (<0.01 wt. %).

Fluid Sr-isotope analysis

Thirty-one hydrothermal fluid samples for Sr isotope analysis were collected in 1995 and 2003 from high-temperature vents along the Endeavour segment using titanium syringe major samplers and the Hydrothermal Fluid and Particle Sampler (Butterfield et al., 2004). Sub-samples for Sr isotope analysis were stored in acid-cleaned HDPE bottles and acidified with ultra-pure HCl to pH <2. Strontium isotope compositions of fluids were analyzed by thermal ionization mass spectrometry at the University of Washington with methods described by Nelson (1995). Magnesium concentration was determined by ion chromatography (precision 1%). Strontium concentration in vent fluids was determined by atomic absorption spectrophotometry (precision 4%).

Whole-rock Sr-isotope analysis

The bulk strontium isotope ($^{87}\text{Sr}/^{86}\text{Sr}$) composition of 16 barite-rich samples was determined using thermal ionization mass spectrometry. For each analysis, approximately 50 mg of crushed sample was leached in ~2 mL of 7M HNO₃ on a 100°C hot plate in order to dissolve the sulfide minerals. This process was repeated three times in order to ensure complete dissolution of sulfides. The remaining barite crystals were immersed in 6M HCl and left covered on a 100°C hot plate for three days. The solution was then removed by pipette and the samples were left to dry down overnight. Finally, 1.5 mL of 2.5M HCl was added to each solution and the samples were left covered for two days. The solutions containing the dissolved barite were run through Sr resin columns to isolate the Sr. The resulting samples were analyzed using a ThermoFinnigan TRITON thermal ionization multi-collector mass spectrometer at Carleton University. Samples underwent ~100 analyses at 1200-1406°C with a baseline measurement taken after every 10 analyses.

In situ laser ablation analysis

Concentrations of a suite of 61 elements from Sr-rich and Sr-poor zones of a single crystal were measured using a 193 nm Excimer laser ablation system (GeoLasPro, Coherent) coupled to a double-focusing, high-resolution magnetic sector mass spectrometer (AttoM, Nu Instruments) at GEOMAR (Fietzke and Frische, 2016). Individual analyses on the crystal surface consisted of continuous sampling along 100 µm rasters parallel to the mineral zonation at a scan rate of 3 µm/s, with a 32 µm beam width and a fluence of 2 J/cm² at a repetition rate of 10 Hz. Ablation sites were chosen in order to avoid fractures or areas with abundant fluid inclusions. Two standard reference glasses (NIST SRM 612 and 610) and a synthetic sulfide standard (PGE_Ni7b) were used for calibration.

A New Wave UP193 laser, attached to an AXIOM multi-collector inductively-coupled plasma mass spectrometer, also at GEOMAR, was used to measure the $^{87}\text{Sr}/^{86}\text{Sr}$ composition of individual zones within single barite crystals from two samples, including the same crystal

analyzed for trace element abundances. Analyses and data reduction using a LRS (linear regression slope) method followed the approach described by Fietzke et al. (2008).

Single analyses on the crystal surfaces consisted of 100 μm line scan ablations parallel to the Sr zonation using a spot size of 25 μm , fluence of 2 J/cm^2 and repetition rate of 10 Hz at a 3 $\mu\text{m}/\text{s}$ scan speed. Precision and accuracy of the measurements was evaluated by repeat duplicate analysis of a modern marine carbonate reference standard after every fifth analysis. See supplementary information for further analytical details.

Microthermometry

For microthermometry measurements, samples were prepared as ~ 50 μm -thick doubly polished sections mounted with acetone-soluble glue. Samples were removed from the carrier glass using acetone prior to microthermometry measurements. Due to the excellent cleavage of barite, care was taken so that only pristine fluid inclusions distal to internal fractures were selected. Measurements were made using Linkam® THMS 600 heating-freezing stages at GEOMAR and at the Department of Geosciences, University of Kiel. Each apparatus was mounted on a standard petrographic microscope with long working distance optics.

The heating-freezing stages were calibrated using SYNFLINC® synthetic fluid inclusion temperature standards. Accuracy and precision were estimated at ± 0.2 $^{\circ}\text{C}$ near the triple point of CO_2 (± 56.6 $^{\circ}\text{C}$), and better than ± 0.5 $^{\circ}\text{C}$ at other temperatures below ambient. Accuracy and precision for total homogenization measurements were estimated at ± 2 $^{\circ}\text{C}$.

Salinities were calculated using the following equation from Bodnar and Vityk (1994):

$$\text{Salinity (wt.\%)} = -1.78(T_m) + 0.0442(T_m)^2 - 0.000557(T_m)^3 \quad (1)$$

where T_m is the final melting temperature, in degrees Celsius, of the solid phase within the inclusion upon heating from below the freezing point. Formation, or trapping temperatures (T_t) were determined by applying a hydrostatic pressure correction to the homogenization temperatures (T_h), which is defined as the minimum temperature in which a single phase fluid is present in the inclusion. For pressure corrections, isochores were calculated using the FLUIDS software package (Bakker, 2003; Bakker, 2012).

Geochemical Modeling

Concentrations of free barium, strontium, calcium and sulfate, and saturation states of barite, anhydrite and amorphous silica, were determined as a function of temperature assuming mixing of 350 $^{\circ}\text{C}$ vent fluid and seawater (Table 1). Calculations were made using the modeling code EQ3/6 (Wolery, 1992; Wolery and Daveler, 1992) with mineral precipitation and equilibrium between H_2S - SO_4 and CO_2 - CH_4 suppressed. Thermodynamic data used were from

SUPCRT92 (Johnson et al., 1992), with data for MgSO_4 and NaSO_4^- species added (McCollom and Shock, 1997).

Results

Crystal Morphology

Barite within hydrothermal vents at Endeavour occurs as a wide range of crystal habits, from well-formed tabular and bladed crystals to dendritic crystals (Fig. 3). The majority of samples contain barite that is not restricted to a single crystal morphology and crystals with different habits often occur in different areas of a single sample. However, samples can be grouped into four broad morphological categories defined by the dominant morphologies present: 1) well-formed, tabular crystals (Fig. 3A); 2) bladed crystals (Fig. 3B); 3) acicular and/or radiating tapered crystals (Fig. 3C); and 4) dendritic crystals (Fig. 3D). Barite crystals vary in size from <0.1 mm up to 2 mm, and the larger crystals tend to have a more euhedral (tabular or bladed) morphology. Sphalerite and pyrite are the most common sulfide minerals present in barite-rich samples. Sphalerite is the dominant sulfide phase in samples with tabular or bladed barite, whereas pyrite is more common in samples that contain smaller acicular or dendritic barite. Barite typically crystallizes into open pore spaces, precipitating on pre-existing sulfide minerals, with the exception of dendritic barite, which often occurs as outward-facing fans on the exterior of a sample (Fig. 3D). Amorphous silica is generally the only phase that precipitates after barite, although sulfide overgrowth or replacement of relict barite is also present.

Trace element content of barite

Whole rock Ba and Ca concentrations for 335 chimney samples are plotted in Figure 4A (see Supplementary Table S1 for full results). The Ba and Ca concentrations reflect the amount of barite and anhydrite in each sample, respectively, and range from below detection limits up to ~40 wt. % for both elements. The strong negative correlation between Ba and Ca is typical of hydrothermal vents in this and other locations (Hannington et al., 1995; Koski et al., 1994), and reflects the different saturation conditions under which barite and anhydrite precipitate within vents. The whole rock Sr concentrations are plotted against Ba in Figure 4B. The samples are divided into those with either greater than or less than 1 wt. % Ca. For samples with less than 1 wt. % Ca, Sr concentrations range from 0 to 1.3 wt. % and there is a positive correlation between Sr and Ba ($R^2 = 0.74$). Samples that contain more than 1 wt. % Ca are generally Ba-poor, and contain up to only ~0.3 wt. % Sr, but show a similarly strong positive correlation between Ca and Sr ($R^2 = 0.83$). The strong correlations between Sr and both Ba and Ca indicate that barite and anhydrite are the primary mineral phases that host Sr in hydrothermal chimneys at Endeavour. Because Ba-rich samples are generally Ca-poor, the bulk of the Sr within Ba-rich samples will be contained within barite, and thus the reported whole rock $^{87}\text{Sr}/^{86}\text{Sr}$ ratios for

Ba-rich samples are assumed to represent the Sr isotopic composition of barite within these samples.

Electron microprobe analysis of growth zones within individual barite crystals indicate that Sr and Ca are the major trace elements within barite and that the darker chemical zonations visible in the backscatter images reflect higher concentrations of Sr and Ca within the crystals (Fig. 5A and B). Strontium content (reported as percent relative to total Ba+Sr+Ca) ranges from 0% to 18%, with an average of 5.5% from 41 analyses. Calcium values are lower, and range from 0% to 10.9% and averages 1.9% (n = 35) (see Supplementary Table S2 and Figure S1 for full results).

Trace element concentrations from laser ablation analysis of a single barite crystal from ALV2467-R2 are reported in Table 2 (lines A through H in Fig. 5C). Although concentrations of 61 elements were measured, only the elements with values above detection limits are included (see Supplementary Table S3 for results for all elements). The results are similar to the electron microprobe results, and indicate that concentrations of Sr, Ca and K are higher within the darker zones.

Hydrothermal fluid Sr concentrations and $^{87}\text{Sr}/^{86}\text{Sr}$ composition

The zero Mg endmember Sr isotope composition for vent fluids is determined by linear regression of $^{87}\text{Sr}/^{86}\text{Sr}$ ratio with Mg/Sr ratio and extrapolation to zero Mg/Sr (Butterfield et al., 2001). There is minor variation in the $^{87}\text{Sr}/^{86}\text{Sr}$ endmember between vent fields along the axis. When all samples are regressed together, the composite endmember for the whole segment is 0.70343 ± 0.00015 . The majority of fluid samples were taken in the Main Endeavour Field (MEF), potentially biasing the results of the composite regression. When the endmember for each vent field is regressed independently, and then vent field endmembers averaged for the segment, a similar value of 0.70343 ± 0.00011 is obtained. This value is within the uncertainty range of the average $^{87}\text{Sr}/^{86}\text{Sr}$ value of 0.70329 ± 0.00037 (1-sigma) for hydrothermal fluids from mid-ocean ridge-hosted hydrothermal systems, based on measurements from the East Pacific Rise (Von Damm, 1990) and Mid-Atlantic Ridge (Elderfield et al., 1993; Gamo et al., 1996; James et al., 1995; Von Damm, 1990).

Endmember Sr concentrations generally vary with vent fluid chloride concentration (Seyfried et al., 2003). The average Sr concentrations of the endmembers for individual fields (using the same samples used for the Sr isotopic endmember) yields an average Sr concentration of $163 \pm 52 \mu\text{mol/kg}$.

Whole rock $^{87}\text{Sr}/^{86}\text{Sr}$ compositions

Whole rock Sr-isotope ($^{87}\text{Sr}/^{86}\text{Sr}$) ratios for 16 chimney samples are reported in Table 3. Ratios range from 0.703798 to 0.707581 and all fall between the values for Endeavour vent fluids

(0.7034) and modern seawater (0.709183) (Butterfield et al., 2001). Higher $^{87}\text{Sr}/^{86}\text{Sr}$ ratios were generally found in samples dominated by dendritic and acicular barite crystals, whereas lower ratios were typical of samples containing dominantly well-formed, tabular crystals.

$^{87}\text{Sr}/^{86}\text{Sr}$ variations within barite crystals

Results of laser ablation analysis of discrete zones along single barite crystals in samples ALV2464-R4 and ALV2467-R2 are reported in Table 4 and plotted in Figure 6 (locations of analyses are shown in Fig. 5D). For both crystals, there is a clear association between darker zones visible in the backscatter images and higher concentrations of Sr (open blue ovals), similar to the results from electron microprobe analyses.

For ALV2464-R4, $^{87}\text{Sr}/^{86}\text{Sr}$ values along the crystal are, with the exception of lines 16 and 21, within error of each other, and cluster around a value of 0.7046 (green dashed line) which represents the whole rock $^{87}\text{Sr}/^{86}\text{Sr}$ value for this sample (Table 3). Analyses #16 and #21 both sampled fluid inclusion-rich zones within the crystal (appear as dark pits in the backscatter image in Fig. 6). The $^{87}\text{Sr}/^{86}\text{Sr}$ values for these samples are higher than those for the rest of the crystal, suggesting that the inclusions may have trapped fluids that have a higher proportion of seawater than suggested by the surrounding crystal. There is a very weak negative correlation between Sr abundance in the crystal (recorded as Sr-intensity, which represents the relative concentration of Sr based on intensity of the output signal from the mass spectrometer) and $^{87}\text{Sr}/^{86}\text{Sr}$ values (Fig. 7). However, if analyses #16 and #21 are excluded, there is essentially no systematic variation in $^{87}\text{Sr}/^{86}\text{Sr}$ with Sr abundance in the crystal.

For ALV2467-R2, there is a smaller range in $^{87}\text{Sr}/^{86}\text{Sr}$ values than ALV2464-R4, and the values cluster near the whole-rock value of 0.7038 (Fig. 6). A negative correlation between $^{87}\text{Sr}/^{86}\text{Sr}$ values and Sr concentration is slightly more pronounced for this sample (Fig. 7), suggesting that the partitioning of Sr into the barite lattice is greater when the source fluid has a higher proportion of hydrothermally-derived Sr.

Microthermometry

Fluid inclusions were investigated in barite and in interstitial amorphous silica from samples ALV2464-R4 and ALV2467-R2. These samples contain both liquid-dominated and vapour-dominated 2-phase liquid (L) + vapour (V) inclusions at ambient temperatures (Fig. 8). In rare cases, metastable single-phase L inclusions that nucleated a vapour bubble upon cooling below room temperature were encountered. The overall size of individual fluid inclusions ranges from $<1\text{ }\mu\text{m}$ to $\sim 30\text{ }\mu\text{m}$. However, microthermometry measurements were made only on inclusions between 2 and $10\text{ }\mu\text{m}$ in size.

Fluid inclusions within the barite crystals can be texturally classified as either primary or secondary. Primary inclusions occur either as solitary inclusions or small clusters that are well

removed from grain boundaries, or as trails within growth zones of the host mineral that do not approach grain boundaries (Fig. 8A and B). Secondary fluid inclusions occur as trails in healed cracks crosscutting growth zones (if applicable) and ending at the surface boundary of the respective crystal (Fig. 8C). The terms “primary” and “secondary” inclusions as used here apply to single crystals (and in rare cases to their immediate surroundings), and thus do not necessarily imply that all primary inclusions in a given sample were formed earlier than secondary inclusions. Rare fluid inclusions also occur in interstitial spaces between amorphous silica globules (Fig. 8D).

Within each sample, most primary fluid inclusions and many of the secondary inclusions are liquid dominated (i.e. they have vapour bubble sizes comprising less than ~30% of the inclusion volume). A sub-set of secondary inclusions form trails that include vapour-dominated inclusions as well. Careful microscopic investigations indicate that neighbouring liquid-dominated fluid inclusions within many growth zones and secondary trails have variable L/V phase proportions, which is a strong indication of post-entrapment modification upon cooling, involving progressive crack healing, or necking down, after initial bubble formation of the host mineral (Roedder, 1984). Therefore, only inclusion trails where neighbouring inclusions have similar L/V phase proportions, and were therefore assumed to represent the original densities, were selected for microthermometry measurements.

Upon cooling, the liquid-dominated fluid inclusions froze to aggregates of ice and vapour at temperatures between -35 and -55 °C. Once frozen, the vapour bubbles within inclusions containing a vapour phase of less than about 10 vol. % were squeezed out of existence due to expansion of the aqueous phase during the water to ice transition. Further cooling to about -70 to -110 °C produced no further phase changes, implying that gaseous species such as CO₂ or CH₄ can only be present in amounts less than about 5 mole %, if at all (Konnerup-Madsen, 1995). Upon heating the inclusions, initial melting (T_i) occurred between -35 to -21 °C, which is close to the eutectic point in a NaCl-H₂O-dominated system. The lower T_i values suggest the presence of variable amounts of minor species other than NaCl in the system. Final melting temperatures (T_m) for inclusions in barite ranged between -5.4 and -3.5 °C. Using equation (1), final melting temperatures correspond to an average salinity of 7.6 ± 1.1 wt. % NaCl equivalent (1-sigma, $n = 8$) for ALV2464-R4 and 6.6 ± 1.2 wt. % NaCl equivalent (1-sigma, $n = 2$) for ALV2467-R2 (Bakker, 2012; Bodnar and Vityk, 1994) (Table 5). A final melting temperature of -2.0 °C from a single inclusion within amorphous silica from ALV2464-R4 corresponds to a NaCl equivalent salinity of 3.4 wt. %, which is near seawater values (Bakker, 2012; Bodnar and Vityk, 1994).

Final homogenization temperatures of liquid + vapour (L + V) into liquid occur at temperatures between 114 and 269 °C for the dominantly secondary inclusions within barite ($n=64$), and 118

to 127 °C for inclusions within amorphous silica (n=5) (see Supplementary Table S5 for full results). Sample water depths of about 2,200 m corresponds to a pressure of 22 MPa (220 bar), and translates into pressure corrections of 10 to 14 °C and corrected formation temperatures of 124 to 283 °C and 128-137 °C for barite- and amorphous silica-hosted inclusions, respectively (Fig. 9). The highest formation temperatures in both samples correspond to primary inclusions within large, blocky (euhedral) crystals. Lower formation temperatures are associated with secondary liquid dominated inclusions, and primary inclusions in smaller, dendritic crystals.

Due to the small sizes of vapour-dominated inclusions, no exact microthermometry measurements were possible. Melting reactions were visible between 1 and ~10°C in two of the inclusions, which may correspond to melting of a gas hydrate, and thus indicate the presence of a gaseous component like CO₂ or CH₄ in the original vapour phase.

Secondary fluid inclusions are both liquid- and vapour-dominated, indicating that later-stage venting comprised two or more stages, with at least one stage comprising vapour-rich (i.e. low-density) fluids. Formation temperatures for secondary inclusions are typically lower than those for primary inclusions, and cluster between ~130 – 170°C. Secondary inclusions are also found in smaller, less well-formed crystals, which is consistent with results of geochemical modelling that links less well-formed crystals to higher degrees of fluid supersaturation at lower temperatures (see discussion on crystal morphology below). Direct venting of a vapour phase has been reported at Endeavour; however these venting events have been short-lived and associated with episodes of venting of fluids with temperatures at or above the seawater boiling curve (Butterfield et al., 1994; Kelley et al., 2012; Seyfried et al., 2003).

Stretching of barite during heating commonly produces a measurable increase in volume and an increase in homogenization temperature (Ulrich and Bodnar, 1988). This likely accounts for some of the highest homogenization temperatures in Figure 9. However, the results correspond closely to the inferred temperatures of barite formation from both thermal mixing and solubility calculations (see below).

Formation temperatures of 120 – 140°C for amorphous silica are consistent with previous estimates by Tivey and Delaney (1986) and, along with measured fluid salinity near that of seawater, are consistent with precipitation towards the exterior of the chimney walls.

Discussion

Fluid Mixing

The measured ⁸⁷Sr/⁸⁶Sr values within hydrothermal barite in this study (both whole rock and laser ablation spot analyses) lie between the endmember values for seawater and Endeavour hydrothermal fluid (Table 1), and record the amount of mixing between these two endmember

fluids at the sites of barite precipitation within vent chimney walls. The relative contribution of each endmember fluid can be quantified by applying a two component mixing model:

$$\% HF = 100 \times \frac{[Sr]_{SW} \left[\left(\frac{{}^{87}Sr}{{}^{86}Sr} \right)_{SW} - \left(\frac{{}^{87}Sr}{{}^{86}Sr} \right)_{BA} \right]}{[Sr]_{SW} \left[\left(\frac{{}^{87}Sr}{{}^{86}Sr} \right)_{SW} - \left(\frac{{}^{87}Sr}{{}^{86}Sr} \right)_{BA} \right] + [Sr]_{HF} \left[\left(\frac{{}^{87}Sr}{{}^{86}Sr} \right)_{BA} - \left(\frac{{}^{87}Sr}{{}^{86}Sr} \right)_{HF} \right]} \quad (2)$$

where %HF is the proportion of hydrothermal fluid (with the remaining proportion being seawater), $[Sr]_{SW}$ and $[Sr]_{HF}$ are the Sr concentrations of seawater and the hydrothermal fluid, respectively, and $({}^{87}Sr/{}^{86}Sr)_{SW}$, $({}^{87}Sr/{}^{86}Sr)_{HF}$ and $({}^{87}Sr/{}^{86}Sr)_{BA}$ are the Sr-isotope ratios for seawater, hydrothermal fluid and barite, respectively (Mills et al., 1998). This model assumes that there is no fractionation of Sr isotopes during precipitation of barite. An investigation by Widanagamage et al. (2014) of Sr-isotope fractionation during synthetic barite precipitation at temperatures of up to 40°C indicated a maximum fractionation (difference in ${}^{87}Sr/{}^{86}Sr$ between barite and solution) of ~0.0002, which is equivalent to or less than the analytical uncertainty of the measurements presented in this study (Tables 3 and 4). Fractionation factors for barite precipitation in hydrothermal chimneys would likely be much smaller than those reported by Widanagamage et al., due to higher temperatures.

The relative contributions of each endmember fluid that resulted in barite precipitation, based on equation (2), varies from 17 to 88% hydrothermal fluid, and averages 62% (Table 1). For comparison, Kusakabe et al. (1990) report hydrothermal contributions of between 80 and 90% for hydrothermal barite from the Mariana backarc basin using a similar approach. The relative contributions of each endmember fluid can be combined with the physical and chemical properties of the endmember fluids to infer the physical and chemical conditions under which barite precipitated within the chimney walls.

Conditions of barite formation

The fluid temperature within a chimney wall is dependent on the combined effects of the amount of mixing between hot hydrothermal fluid and cold seawater and conductive cooling of the hydrothermal fluid or heating of seawater. If considering only the temperature effects of fluid mixing, the temperature at which barite precipitates can be inferred using a linear thermal mixing relationship:

$$T = X(T_{HF} - T_{SW}) + T_{SW} \quad (3)$$

where T is the temperature of the mixed fluid in degrees Celsius, T_{HF} and T_{SW} are the temperatures of endmember hydrothermal fluid and seawater, respectively, also in degrees Celsius (Table 1), and X is the fraction of hydrothermal fluid in the mixture, calculated using equation (2) (Fig. 10) (Mills and Elderfield, 1995). The endmember hydrothermal fluid

temperature of 350°C represents average typical maximum vent fluid temperatures at Endeavour (Kelley et al., 2012; Seyfried et al., 2003). Temperatures of up to 375°C have been recorded at MEF, and represent the thermodynamic maximum temperature of seawater defined by the hydrostatic pressure at that depth (220 bars at 2,200 m), suggesting that these fluids are on the liquid-vapour phase boundary for seawater (Bischoff and Rosenbauer, 1985; Delaney et al., 1992; Kelley et al., 2012; Tivey et al., 1990). A short-lived episode of higher fluid temperatures (>400°C) has been reported for the MEF, and is thought to represent a brief period of venting of a vapour phase (Butterfield et al., 1994; Tivey et al., 1990).

Calculated mixing temperatures using equation (3) range from 61 to 308 °C for 16 samples from the Endeavour Segment (Table 3). These values are comparable to previous estimates of the temperature range under which hydrothermal barite typically precipitates on the seafloor (e.g., ~100 – 300 °C) (Blount, 1977; Hannington et al., 1995).

The primary inclusions in the larger euhedral crystals of barite are liquid-dominated, indicating barite precipitation from a homogenous, high-density fluid. Trapping temperatures of the majority of the primary inclusions in the large crystals suggest likely barite formation at temperatures of between 180 and 240°C (Fig. 9). These formation temperatures are consistent with previously reported temperatures for barite precipitation (e.g., Halbach et al., 1989; Hannington et al., 1995; Hannington and Scott, 1988), with the highest measured trapping temperatures possibly a result of stretching effects on the inclusions (Ulrich and Bodnar, 1988).

Measured fluid salinities from primary inclusions in barite from samples ALV2467-R2 and ALV2464-R4 are higher than that of seawater, suggesting that the vent fluid contained a component of a brine phase during barite formation for both samples (Coumou et al., 2009). Using the % hydrothermal fluids determined using bulk $^{87}\text{Sr}/^{86}\text{Sr}$ (summarized in Table 3), and a seawater salinity of 3.3 wt. %, the average salinity of 7.6 wt. % NaCl equivalent from sample ALV2464-R4 corresponds to a hydrothermal fluid with a salinity of 9.4 wt.%. For ALV2467-R2, the calculated hydrothermal fluid salinity is 7.1 wt. %. Phase separation is generally accepted to be an important control on fluid chemistry at MEF and High Rise; however, so far only venting of low-salinity fluids has provided any direct evidence of phase separation in the subsurface at these sites (Butterfield et al., 1994; Kelley et al., 2012; Seyfried et al., 2003). Venting of a high-salinity fluid has not been documented at MEF or High Rise, but the presence of a brine layer in the subsurface is predicted from mass-balance constraints (Butterfield et al., 1994; Seyfried et al., 2003) and from time-series temperature-salinity data (Larson et al., 2009). The high-salinity fluid inclusions presented here may be the first evidence of past venting of a high-salinity brine component at MEF and High Rise. The fluid inclusion temperature and salinity data from multiple chimneys suggest an overall early stage of higher-temperature barite precipitation

from a homogenous, high-salinity fluid, followed by later-stage of lower temperature venting of an alternating low-density fluid (vapour phase) and a homogenous high-salinity fluid.

For samples ALV2464-R4 and ALV2467-R2, the calculated fluid inclusion trapping temperatures are lower than the predicted temperatures from fluid mixing by 56 and 119 °C, respectively. Conductive cooling within the chimney walls will result in fluid temperatures being lower than the value calculated based purely on fluid mixing (Hannington and Scott, 1988). If the calculated trapping temperatures from the fluid inclusion microthermometry are considered to represent the actual temperatures of barite precipitation, the temperature difference between the two methods represents the amount of conductive cooling of the hydrothermal fluid within the chimney walls. Hannington and Scott (1988) estimated a decrease in fluid temperature of 75°C (from 350°C to ~275°C) from conductive cooling, followed by mixing with 50% seawater, allowing for the co-precipitation of barite and silica at 185°C within the wall of a hydrothermal spire from Axial Seamount, which is also on the Juan de Fuca Ridge.

Geochemical modelling

The saturation state of the mixed fluid with respect to barite (and other minerals) at different stages of mixing and for different temperatures, fluid compositions and chemical speciation can be inferred from geochemical modelling of the mixing between Endeavour hydrothermal fluid and seawater (Fig. 10). Figure 10A shows variation in the total concentrations of free- and total-dissolved Ba^{2+} , Sr^{2+} , and SO_4^{2-} as a function of both temperature and degree of mixing, using fluid properties summarized in Table 1. The concentrations of free species represent the amount of solute available for mineral precipitation. Ba^{2+} is the dominant barium species in the mixed fluid, especially at lower temperatures. At temperatures above ~200°C, the relative abundance of BaCl^+ increases and the absolute concentration of Ba^{2+} begins to decrease, even though the total Ba in the fluid increases towards higher temperatures. Strontium follows a similar pattern, although, unlike Ba, higher concentrations of Sr are maintained at lower temperatures due to the relatively high abundance of dissolved Sr in seawater. The high concentration of SO_4^{2-} at low temperatures reflects the relatively high concentrations of sulfate in seawater and negligible sulfate in the hydrothermal fluid. However, the slightly irregular surface of the concentration profile in Figure 10A is a result of the complex speciation of sulfate, involving several different cations (Fig. 10B). In particular, the sudden dip in free SO_4^{2-} concentration at ~100°C is associated with greater amounts of NaSO_4^- .

The physicochemical conditions for precipitation or dissolution of barite can be quantified by determining the saturation index of the fluid ($\text{S.I.} = \log Q/K$, where Q is the activity product and K is the equilibrium constant). An $\text{S.I.} > 0$ will result in mineral precipitation, and a $\text{S.I.} < 0$ will result in mineral dissolution. Saturation indices for barite, anhydrite and amorphous silica are plotted in Figure 10C. According to the model, barite will precipitate from mixing fluid at

temperatures of between ~5 and 330°C. These temperatures correspond to fluid mixtures that contain as little as 1% hydrothermal fluid, and as much as 94% hydrothermal fluid, reflecting the very low solubility of barite. Anhydrite will precipitate from the fluid at mixing temperatures greater than ~120°C. The model predicts that amorphous silica, which is often abundant within Endeavour hydrothermal vents (e.g., Fig 2A) will never reach saturation and will not precipitate solely as a result of fluid mixing. The mixing model does not consider conductive cooling, which is required for precipitation of amorphous silica, but the effect on barite saturation can be inferred from Figure 10. If parcels of mixed fluid cool conductively, the saturation index of barite would increase because free Ba^{2+} and free SO_4^{2-} in the mixed fluid would increase as the stabilities of NaSO_4^- and BaCl^+ complexes decrease at lower temperatures.

The modeling results presented in Figure 10 also do not consider the effects of mineral precipitation on fluid composition and saturation index. Because of the high degree of supersaturation of anhydrite relative to barite at high temperatures (Fig. 10C), anhydrite precipitation would remove sulfate from the solution within a chimney, inhibiting the precipitation of barite at these high temperatures, resulting in the typical association of anhydrite with high-temperature sulfide minerals (e.g., chalcopyrite, pyrrhotite) in the interior and barite with lower-temperature sulfide minerals (pyrite, sphalerite) towards the exterior of a chimney (Hannington et al., 1995).

The Ba concentration of the hydrothermal fluid reported in Table 1 represents the maximum reported non-endmember value for the Main Endeavour Field. Because of its very low solubility, precipitation of barite reduces the amount of dissolved Ba during fluid sampling, and results in non-linear behavior when determining zero-Mg endmember values and, for this reason, endmember Ba concentrations are rarely reported (Seyfried et al., 2003). The concentration of Ba within Endeavour hydrothermal fluid is likely higher than the maximum reported value of 31 $\mu\text{mol/L}$ (Seyfried et al., 2003). Reported endmember Ba concentrations at Lucky Strike, another E-MORB-hosted hydrothermal site, are comparable and range between 10 and 52 $\mu\text{mol/L}$ (Charlou et al., 2000). However, in this case the authors also state that the reported concentrations likely represent minimum values. The highest reported endmember Ba concentration for a vent fluid is 119 $\mu\text{mol/L}$, from fluids sampled from the Edmond site, on the Central Indian Ridge (Kumagai et al., 2008). The high values at this site are also attributed to enriched Ba within the underlying source rocks. Whether or not this maximum reported concentration is representative of the actual endmember concentration is unclear. However, this value does point to the possibility of Ba concentrations at Endeavour (and other mid-ocean ridge hydrothermal sites) being significantly higher than the reported non-endmember values for Endeavour fluids. Even at endmember concentrations double the amount indicated in Table 1, barite precipitation is predicted to occur over roughly the same temperature range (Figure

10C). The geochemical modelling confirms that Ba concentration is the limiting factor during barite precipitation in any fluid mixture that contains an excess of sulfate (the intersection of the Ba^{2+} and SO_4^{2-} curves in Fig. 10A).

Crystal Morphology

Laboratory growth experiments have linked barite crystal morphology to crystal growth rates and the degree of supersaturation of Ba^{2+} and SO_4^{2-} in the crystallizing fluid (Judat and Kind, 2004; Li et al., 2007; Shikazono, 1994; Widanagamage et al., 2014). Dendritic crystals grow quickly as a result of diffusion-limited aggregation of solute atoms from highly supersaturated fluids (Turcotte, 1997). Well-formed crystals grow more slowly at lower degrees of supersaturation, predominantly from surface reaction precipitation mechanisms (Shikazono, 1994).

A comparison of dominant barite crystal morphology for samples from Endeavour with the degree of fluid mixing and S.I. (Fig. 10C; Table 3) shows a relationship consistent with the experimental results described above. A marked increase in S.I. occurs at temperatures between ~10 and 140°C, which corresponds to greater free SO_4^{2-} concentration and coincides with a marked decrease in the stability of NaSO_4^- . The single sample that plots in this region (ALV1452-1A) contains mainly dendritic barite, which is generally in agreement with the experimental results of Shikazono (1994), although the magnitude of supersaturation is significantly less. This is likely a result of the highly dynamic fluid environment within a vent chimney wall as compared to static laboratory experiments. Shikazono (1994) demonstrated that, under static laboratory conditions of 150°C and pressures equal to the vapour pressures of the aqueous solutions, barite that precipitates from a solution with an S.I. below 20 will result in well-formed barite crystals. Dendritic crystals will form from a solution with an S.I. larger than 20 (i.e. a higher degree of supersaturation). The results from this study suggest that, in the dynamic environment within vent chimney walls, dendritic barite forms at low temperatures and high inputs of seawater, resulting in a S.I. of above ~0.6. This relationship is consistent with the typical occurrence of dendritic barite along the outer margins of a vent (e.g., Fig. 3D).

Strontium partitioning

The degree of Sr substitution in barite, expressed as an apparent partition coefficient ($K_D = (\text{Sr}/\text{Ba})_{\text{barite}}/(\text{Sr}/\text{Ba})_{\text{fluid}}$), was calculated for individual samples using whole rock geochemical data and modelled fluid compositions (Table 3). Calculated K_D values are reported as “apparent” values because the rapid temperature changes and high fluid flow velocities associated with hydrothermal venting, as well as the occurrence of dendritic crystal morphologies associated with high degrees of supersaturation, indicate non-equilibrium conditions during barite crystallization (Shikazono, 1994). Trace element substitution within

crystals is controlled by the composition of the crystallizing fluid, pressure, temperature and crystal growth rate (Averyt and Paytan, 2003; Hannington and Scott, 1988; Sasaki and Minato, 1983). However, the effects of these external factors on element partitioning within barite under hydrothermal conditions are not well constrained (Shikazono et al., 2012). Laboratory experiments and thermodynamic constraints for typical marine conditions (i.e. low-temperature) indicate that Sr substitution in barite increases with temperature (Averyt and Paytan, 2003; Hanor, 2000). Alternatively, under hydrothermal conditions, Shikazono et al. (2012) link increased Sr partitioning to higher degrees of supersaturation and fast crystal growth. Sasaki and Minato (1983) suggest that, from precipitation experiments at temperatures between ~25 and 60°C, the degree of supersaturation has a stronger control on Sr partitioning than temperature. A comparison of Sr/Ba ratios to apparent partition coefficient shows no relationship between degree of mixing and Sr substitution, indicating that different degrees of mixing, and hence fluid composition, are not a primary control on Sr substitution (Fig. 11B).

Apparent partition coefficients for individual Sr-rich and Sr-poor zones within a single crystal were also determined using crystal chemistry derived from laser ablation (Table 2) and modeled fluid compositions (Table 6; Fig. 11B). The consistent $^{87}\text{Sr}/^{86}\text{Sr}$ across individual Sr-rich and Sr-poor growth zones (Fig. 6) provide further evidence that Sr partitioning in the barite is not controlled by fluid mixing. The pattern of Ca substitution mimics that of Sr, which suggests that the zonation is also not solely a result of temporal variations in fluid Sr concentrations. Butterfield et al. (1994) report remarkably stable vent fluid chemistry at MEF over a 4-year period, although Lilley et al., (2003) and Seewald et al., (2003) report rapid changes in salinity in MEF following earthquakes and inferred magmatic activity. The higher abundance of fluid inclusions within the darker growth zones suggests that higher degrees of Sr substitution reflect periods of faster crystal growth, driven by increased conductive cooling and a higher degree of supersaturation. Changes in the amount of conductive cooling could result from oscillations in hydrothermal fluid flux. Without information on crystal growth rates, it is difficult to evaluate how much time is represented by each growth zone. However, the sharp boundaries between zones and oscillatory nature of the zonations suggest that the environmental factor(s) responsible for the zonations occur quickly and cyclically. The lighter zones are generally larger than the darker zones. This, coupled with the fact that crystal growth is likely faster during formation of the darker zones, indicates that conditions that favour lower levels of Sr substitution (i.e. the lighter zones; Fig 5B) during crystal growth occur over longer periods of time than conditions that favour higher levels of Sr substitution.

Conclusions

The results of this study illustrate the utility of barite for recording physical and chemical processes associated with the formation of seafloor hydrothermal sulfide deposits. Specifically, barite records the temperature and chemical conditions that occur within vent chimney walls as a result of fluid mixing and conductive cooling. The occurrence of different crystal habits of barite within different parts of a chimney can provide a first order visual or petrographic tool for assessing the geochemical environment within chimney walls during active venting. A two-component mixing model based on $^{87}\text{Sr}/^{86}\text{Sr}$ compositions of barite from hydrothermal vents on the Endeavour Segment provides an effective means for quantifying the amount of fluid mixing that occurs within chimney walls. Results of Sr-isotope analyses indicate that, due to the very low solubility of barite, precipitation can occur over a wide range of mixing of hydrothermal fluid and seawater, with as little as a 17% hydrothermal fluid to as much as 88% hydrothermal fluid, and barite can precipitate at any stage during the growth history of a hydrothermal vent.

Precipitation of barite is controlled largely by the availability of free Ba^{2+} in the fluid mixture. High degrees of supersaturation associated with higher proportions of seawater result in crystal growth that is dominated by acicular and dendritic morphologies. Large, tabular and bladed crystals occur in more Ba-limited conditions in the interior regions of chimneys. Large euhedral crystals form at temperatures between ~ 120 and 240°C , which are consistent with previous estimates for hydrothermal barite. A comparison of formation temperatures with modeled temperatures based on fluid mixing indicate that conductive cooling lowers the temperatures within the chimney walls by 60 to 120°C , which will enhance barite precipitation.

Barite crystals also provide an effective record of fluid composition within chimney walls. Strontium zonation within single barite crystals that were originally thought to represent changes in fluid chemistry during crystal growth are instead attributed to temperature fluctuations, and indicate that fluid chemistry is relatively stable over the growth periods of single crystals. Fluid salinity measurements from fluid inclusions trapped within barite crystals provide the first direct evidence of past venting of a fluid with a brine component from the Main Endeavour Field.

Unlike anhydrite, which has also been the focus of fluid mixing studies, barite is preserved on the seafloor and provides a record of fluid interaction in deposits from extinct hydrothermal systems on the seafloor and even ancient hydrothermal deposits on obducted oceanic crust. The physicochemical information recorded within barite that is outlined in this study can be used to evaluate the microbial habitat conditions and hydrothermal fluid properties in extinct deposits (e.g., Golding et al., 2011; Rasmussen, 2000). Comparative studies with barite hosted within ancient deposits may provide insights into ancient ocean chemistry and the formation of volcanogenic massive sulfide deposits (e.g., Jamieson et al., 2013b; Vearncombe et al., 1995).

Acknowledgements

The authors would like to thank Mario Thoner (GEOMAR) and Peter Jones (Carleton University) for their help collecting electron microprobe data, Elizabeth Ann Spencer (Carleton University) for help collecting Sr-isotope data, and Sven Petersen for many thoughtful discussions on hydrothermal chimney formation. Cora C. Wohlgemuth-Ueberwasser (Stockholm University) is gratefully acknowledged for providing the sulfide standard for laser ablation analysis. This work was supported by an NSERC PGS scholarship to JWW and NSERC Discovery Grant to MDH. MKT acknowledges funding from NSF OCE- 1130019. DAB acknowledges funding from NSF OCE- 0731947 and the Joint Institute for the Study of the Atmosphere and Ocean (JISAO) under NOAA Cooperative Agreement NA10OAR4320148, contribution No. 2472, PMEL contribution No. 4399.

References

- Albarede, F., Michard, A., Minster, J.F., Michard, G., 1981. Sr-87-Sr-86 ratios in hydrothermal waters and deposits from the East Pacific Rise at 21-Degrees-North. *Earth and Planetary Science Letters* 55, 229-236.
- Averyt, K.B., Paytan, A., 2003. Empirical partition coefficients for Sr and Ca in marine barite: Implications for reconstructing seawater Sr and Ca concentrations. *Geochemistry Geophysics Geosystems* 4.
- Baker, E., German, C., Elderfield, H., 1995. Hydrothermal plumes over spreading center axes: Global distribution and geological inferences. *Geophysical Monograph* 91, 47-71.
- Bakker, R.J., 2003. Package FLUIDS 1. Computer programs for analysis of fluid inclusion data and for modelling bulk fluid properties. *Chemical Geology* 194, 3-23.
- Bakker, R.J., 2012. Package FLUIDS. Part 4: thermodynamic modelling and purely empirical equations for H₂O-NaCl-KCl solutions. *Mineralogy and Petrology* 105, 1-29.
- Bischoff, J.L., Rosenbauer, R.J., 1985. An empirical-equation of state for hydrothermal seawater (3.2-percent NaCl). *American Journal of Science* 285, 725-763.
- Blount, C.W., 1977. Barite solubilities and thermodynamic quantities up to 300-degrees-C and 1400 bars. *American Mineralogist* 62, 942-957.
- Bodnar, R., Vityk, M., 1994. Interpretation of microthermometric data for H₂O-NaCl Fluid Inclusions, in: De Vivo, B., Frezzotti, M. (Eds.), *Fluid Inclusions in Minerals, Methods and Applications*. Virginia Tech, Blacksburg, VA, pp. 117-130.
- Butterfield, D.A., Lilley, M.D., Huber, J.A., Roe, K.K., Embley, R.E., Baross, J.A., Massoth, G.J., 2004. Mixing, Reaction and Microbial Activity in the Sub-seafloor Revealed by Temporal and Spatial Variation in Diffuse Flow Vents at Axial Volcano, in: Wilcock, W.S.D., Kelley, D.S., Baross, J.A., DeLong, E., Cary, C. (Eds.), *The Sub-seafloor Biosphere at Mid-ocean Ridges*. American Geophysical Union.
- Butterfield, D.A., McDuff, R.E., Mottl, M.J., Lilley, M.D., Lupton, J.E., Massoth, G.J., 1994. Gradients in the composition of hydrothermal fluids from the Endeavour Segment vent field - Phase-separation and brine loss. *Journal of Geophysical Research-Solid Earth* 99, 9561-9583.
- Butterfield, D.A., Nelson, B.K., Wheat, C.G., Mottl, M.J., Roe, K.K., 2001. Evidence for basaltic Sr in midocean ridge-flank hydrothermal systems and implications for the global oceanic Sr isotope balance. *Geochimica Et Cosmochimica Acta* 65, 4141-4153.
- Chan, L.H., Edmond, J.M., Stallard, R.F., Broecker, W.S., Chung, Y.C., Weiss, R.F., Ku, T.L., 1976. Radium and barium at GEOSECS stations in Atlantic and Pacific. *Earth and Planetary Science Letters* 32, 258-267.

- Charlou, J.L., Donval, J.P., Douville, E., Jean-Baptiste, P., Radford-Knoery, J., Fouquet, Y., Dapoigny, A., Stievenard, M., 2000. Compared geochemical signatures and the evolution of Menez Gwen (37 degrees 50 ' N) and Lucky Strike (37 degrees 17 ' N) hydrothermal fluids, south of the Azores Triple Junction on the Mid-Atlantic Ridge. *Chemical Geology* 171, 49-75.
- Clague, D.A., Caress, D.W., Thomas, H., Thompson, D., Calarco, M., Holden, J., Butterfield, D., 2008. Abundance and distribution of hydrothermal chimneys and mounds on the Endeavour Ridge determined by 1-m resolution AUV multibeam mapping surveys. *Eos, Transactions, American Geophysical Union* 89.
- Coumou, D., Driesner, T., Weis, P., Heinrich, C.A., 2009. Phase separation, brine formation, and salinity variation at Black Smoker hydrothermal systems. *Journal of Geophysical Research-Solid Earth* 114.
- Cousens, B., 2010. Igneous Rock Associations 11. The Geology and Petrology of Seafloor Volcanic Rocks of the Northeastern Pacific Ocean, Offshore Canada. *Geoscience Canada* 37, 49-64.
- de Ronde, C.E.J., Hannington, M.D., Stoffers, P., Wright, I.C., Ditchburn, R.G., Reyes, A.G., Baker, E.T., Massoth, G.J., Lupton, J.E., Walker, S.L., Greene, R.R., Soong, C.W.R., Ishibashi, J., Lebon, G.T., Bray, C.J., Resing, J.A., 2005. Evolution of a submarine magmatic-hydrothermal system: Brothers volcano, southern Kermadec arc, New Zealand. *Economic Geology* 100, 1097-1133.
- Delaney, J.R., Robigou, V., McDuff, R.E., Tivey, M.K., 1992. Geology of a vigorous hydrothermal system on the Endeavour Segment, Juan de Fuca Ridge. *Journal of Geophysical Research-Solid Earth* 97, 19663-19682.
- Ditchburn, R., Graham, I., Barry, B., de Ronde, C., 2004. Uranium series disequilibrium dating of black smoker chimneys. *New Zealand Science Reviews* 61, 54-56.
- Ditchburn, R.G., de Ronde, C.E.J., Barry, B.J., 2012. Radiometric Dating of Volcanogenic Massive Sulfides and Associated Iron Oxide Crusts with an Emphasis on Ra-226/Ba and Ra-228/Ra-226 in Volcanic and Hydrothermal Processes at Intraoceanic Arcs. *Economic Geology* 107, 1635-1648.
- Elderfield, H., Mills, R.A., Rudnicki, M.D., 1993. Geochemical and thermal fluxes, high-temperature venting and diffuse flow from mid-ocean ridge systems: the TAG hydrothermal field, Mid-Atlantic Ridge 26°N. *Geological Society of London Special Publication* 76, 295-307.
- Fietzke, J., Frische, M., 2016. Experimental evaluation of elemental behavior during LA-ICP-MS: influences of plasma conditions and limits of plasma robustness. *Journal of Analytical Atomic Spectrometry*, DOI: 10.1039/c5ja00253b.
- Fietzke, J., Liebetrau, V., Guenther, D., Guers, K., Hametner, K., Zumholz, K., Hansteen, T.H., Eisenhauer, A., 2008. An alternative data acquisition and evaluation strategy for improved isotope ratio precision using LA-MC-ICP-MS applied to stable and radiogenic strontium isotopes in carbonates. *Journal of Analytical Atomic Spectrometry* 23, 955-961.
- Gamo, T., Chiba, H., Masuda, H., Edmonds, H.N., Fujioka, K., Kodama, Y., Nanba, H., Sano, Y., 1996. Chemical characteristics of hydrothermal fluids from the TAG mound of the Mid-Atlantic Ridge in August 1994: Implications for spatial and temporal variability of hydrothermal activity. *Geophysical Research Letters* 23, 3483-3486.
- Glickson, D.A., Kelley, D.S., Delaney, J.R., 2006. The Sasquatch Hydrothermal Field: Linkages Between Seismic Activity, Hydrothermal Flow, and Geology. *American Geophysical Union, Fall Meeting 2006 Abstract #V23B-0614*.
- Glickson, D.A., Kelley, D.S., Delaney, J.R., 2007. Geology and hydrothermal evolution of the Mothra Hydrothermal Field, Endeavour Segment, Juan de Fuca Ridge. *Geochemistry Geophysics Geosystems* 8.
- Golding, S.D., Duck, L.J., Young, E., Baublys, K.A., Glikson, M., Kamber, B.S., 2011. Earliest Seafloor Hydrothermal Systems on Earth: Comparison with Modern Analogues, in: Golding, S.D., Glikson, M. (Eds.), *Earliest Life on Earth: Habitats, Environments and Methods of Detection*. Springer Netherlands, Amsterdam, Netherlands, pp. 15-49.

- Goldstein, S.J., Murrell, M.T., Janecky, D.R., Delaney, J.R., Clague, D.A., 1991. Geochronology and petrogenesis of MORB from the Juan de Fuca and Gorda Ridges by U-238 Th-230 disequilibrium. *Earth and Planetary Science Letters* 107, 25-41.
- Halbach, P., Nakamura, K., Wahsner, M., Lange, J., Sakai, H., Kaselitz, L., Hansen, R.D., Yamano, M., Post, J., Prause, B., Seifert, R., Michaelis, W., Teichmann, F., Kinoshita, M., Marten, A., Ishibashi, J., Czerwinski, S., Blum, N., 1989. Probably modern analog of Kuroko-type massive sulfide deposits in the Okinawa Trough back-arc basin. *Nature* 338, 496-499.
- Halevy, I., Peters, S.E., Fischer, W.W., 2012. Sulfate Burial Constraints on the Phanerozoic Sulfur Cycle. *Science* 337, 331-334.
- Hannington, M., De Ronde, C., Petersen, S., 2005. Sea-Floor Tectonics and Submarine Hydrothermal Systems. *Economic Geology 100th Anniversary Volume*, pp. 111-141.
- Hannington, M., Herzig, P., Scott, S., Thompson, G., Rona, P., 1991. Comparative mineralogy and geochemistry of gold-bearing sulfide deposits on the midocean ridges. *Marine Geology* 101, 217-248.
- Hannington, M., Jonasson, I., Herzig, P., Petersen, S., 1995. Physical and chemical processes of seafloor mineralization at mid-ocean ridges. *Geophysical Monograph* 11, 115-157.
- Hannington, M.D., Scott, S.D., 1988. Mineralogy and geochemistry of a hydrothermal silica sulfide sulfate spire in the caldera of Axial Seamount, Juan-de-Fuca Ridge. *Canadian Mineralogist* 26, 603-625.
- Hanor, J.S., 2000. Barite-celestine geochemistry and environments of formation. *Sulfate Minerals - Crystallography, Geochemistry and Environmental Significance* 40, 193-275.
- Humphris, S.E., Bach, W., 2005. On the Sr isotope and REE compositions of anhydrites from the TAG seafloor hydrothermal system. *Geochimica et Cosmochimica Acta* 69, 1511-1525.
- James, R.H., Elderfield, H., Palmer, M.R., 1995. The chemistry of hydrothermal fluids from the Broken Spur site, 29-degrees-N Mid-Atlantic Ridge. *Geochimica Et Cosmochimica Acta* 59, 651-659.
- Jamieson, J.W., Clague, D.A., Hannington, M.D., 2014. Hydrothermal sulfide accumulation along the Endeavour Segment, Juan de Fuca Ridge *Earth and Planetary Science Letters* 395, 136-148.
- Jamieson, J.W., Hannington, M.D., Clague, D.A., Kelley, D.S., Delaney, J.R., Holden, J.F., Tivey, M.K., Kimpe, L.E., 2013a. Sulfide geochronology along the Endeavour Segment of the Juan de Fuca Ridge. *Geochemistry Geophysics Geosystems* 14, 2084-2099.
- Jamieson, J.W., Wing, B.A., Farquhar, J., Hannington, M.D., 2013b. Neoarchaeon seawater sulphate concentrations from sulphur isotopes in massive sulphide ore. *Nature Geoscience* 6, 61-64.
- Johnson, J.W., Oelkers, E.H., Helgeson, H.C., 1992. SUPCRT92 - A software package for calculating the standard molal thermodynamic properties of minerals, gases, aqueous species, and reactions from 1-bar to 5000-bar and 0-degrees-C to 1000-degrees-C. *Computers & Geosciences* 18, 899-947.
- Judat, B., Kind, M., 2004. Morphology and internal structure of barium sulfate - derivation of a new growth mechanism. *Journal of Colloid and Interface Science* 269, 341-353.
- Karsten, J.L., Delaney, J.R., Rhodes, J.M., Lias, R.A., 1990. Spatial and temporal evolution of magmatic systems beneath the Endeavour Segment, Juan de Fuca Ridge - Tectonic and petrologic constraints. *Journal of Geophysical Research-Solid Earth and Planets* 95, 19235-19256.
- Kelley, D.S., Carbotte, S.M., Caress, D.W., Clague, D.A., Delaney, J.R., Gill, J.B., Hadaway, H., Holden, J.F., Hooft, E.E.E., Kellogg, J.P., Lilley, M.D., Stoermer, M., Toomey, D., Weekly, R., Wilcock, W.S.D., 2012. Endeavour Segment of the Juan de Fuca Ridge One of the most remarkable places on Earth. *Oceanography* 25, 44-61.
- Kelley, D.S., Delaney, J.R., Yoerger, D.R., 2001. Geology and venting characteristics of the Mothra hydrothermal field, Endeavour segment, Juan de Fuca Ridge. *Geology* 29, 959-962.

- Kim, K.H., McMurtry, G.M., 1991. Radial growth-rates and Pb-210 ages of hydrothermal massive sulfides from the Juan de Fuca Ridge. *Earth and Planetary Science Letters* 104, 299-314.
- Konnerup-Madsen, J., 1995. Basic microthermometry observations on fluid inclusions in minerals - a working manual. Geologisk Institut, Copenhagen.
- Koski, R.A., Jonasson, I.R., Kadko, D.C., Smith, V.K., Wong, F.L., 1994. Compositions, growth mechanisms, and temporal relations of hydrothermal sulfide-sulfate-silica chimneys at the northern Cleft Segment, Juan de Fuca Ridge. *Journal of Geophysical Research-Solid Earth* 99, 4813-4832.
- Kristall, B., Kelley, D.S., Hannington, M.D., Delaney, J.R., 2006. Growth history of a diffusely venting sulfide structure from the Juan de Fuca Ridge: A petrological and geochemical study. *Geochemistry Geophysics Geosystems* 7.
- Kumagai, H., Nakamura, K., Toki, T., Morishita, T., Okino, K., Ishibashi, J.I., Tsunogai, U., Kawagucci, S., Gamo, T., Shibuya, T., Sawaguchi, T., Neo, N., Joshima, M., Sato, T., Takai, K., 2008. Geological background of the Kairei and Edmond hydrothermal fields along the Central Indian Ridge: Implications of their vent fluids' distinct chemistry. *Geofluids* 8, 239-251.
- Kusakabe, M., Mayeda, S., Nakamura, E., 1990. S, O and Sr isotope systematic of active vent materials from the Mariana Backarc Basin spreading axis at 18-degrees-N. *Earth and Planetary Science Letters* 100, 275-282.
- Larson, B.I., Lilley, M.D., Olson, E.J., 2009. Parameters of subsurface brines and hydrothermal processes 12-15 months after the 1999 magmatic event at the Main Endeavor Field as inferred from in situ time series measurements of chloride and temperature. *Journal of Geophysical Research-Solid Earth* 114.
- Li, S.W., Xu, J.H., Luo, G.S., 2007. Control of crystal morphology through supersaturation ratio and mixing conditions. *Journal of Crystal Growth* 304, 219-224.
- Lilley, M.D., Butterfield, D.A., Lupton, J.E., and Olson, E.J. 2003 Magmatic events can produce rapid changes in hydrothermal vent chemistry. *Nature*, 422, 878-881.
- Lilley, M.D., Butterfield, D.A., Olson, E.J., Lupton, J.E., Macko, S.A., McDuff, R.E., 1993. Anomalous CH₄ and NH₄⁺ concentrations at an unsedimented mid-ocean-ridge hydrothermal system. *Nature* 364, 45-47.
- McCollom, T.M., Shock, E.L., 1997. Geochemical constraints on chemolithoautotrophic metabolism by microorganisms in seafloor hydrothermal systems. *Geochimica Et Cosmochimica Acta* 61, 4375-4391.
- Mills, R., Teagle, D., Tivey, M., 1998. Fluid mixing and anhydrite precipitation within the TAG mound, in: Herzig, P., Humphris, S., Miller, D., Zierenberg, R. (Eds.), *Proceedings of the Ocean Drilling Program, Scientific Results*. Vol. 158, Ocean Drilling Program, College Station, TX, pp. 119-127.
- Mills, R.A., Elderfield, H., 1995. Rare-earth element geochemistry of hydrothermal deposits from the active TAG mound, 26-degrees-N Mid-Atlantic Ridge. *Geochimica Et Cosmochimica Acta* 59, 3511-3524.
- Nelson, B.K., 1995. Fluid-flow in subduction zones - evidence from Nd and Sr-isotope variations in metabasalts of the Franciscan Complex, California. *Contributions to Mineralogy and Petrology* 119, 247-262.
- Proskurowski, G., Lilley, M.D., Brown, T.A., 2004. Isotopic evidence of magmatism and seawater bicarbonate removal at the endeavour hydrothermal system. *Earth and Planetary Science Letters* 225, 53-61.
- Rasmussen, B., 2000. Filamentous microfossils in a 3,235-million-year-old volcanogenic massive sulphide deposit. *Nature* 405, 676-679.
- Riddihough, R., 1984. Recent movements of the Juan-de-Fuca plate system. *Journal of Geophysical Research* 89, 6980-6994.

- Robigou, V., Delaney, J.R., Stakes, D.S., 1993. Large massive sulfide deposits in a newly discovered active hydrothermal system, the Highrise Field, Endeavour Segment, Juan-de-Fuca Ridge. *Geophysical Research Letters* 20, 1887-1890.
- Roedder, E., 1984. Fluid Inclusions. *Reviews in Mineralogy* 12, 1-&.
- Ruiz-Agudo, C., Putnis, C.V., Ruiz-Agudo, E., Putnis, A., 2015. The influence of pH on barite nucleation and growth. *Chemical Geology* 391, 7-18.
- Sasaki, N., Minato, H., 1983. Effect of the degree of supersaturation upon apparent partition coefficients of lead and strontium ions between BaSO₄ and aqueous solution. *Mineralogical Journal* 11, 365-381.
- Seewald, J., Cruse, A., Saccocia, P., 2003. Aqueous volatiles in hydrothermal fluids from Main Endeavour Field, northern Juan de Fuca Ridge: temporal variability following earthquake activity. *Earth Planet. Sci. Lett.*, 216, 575-590.
- Seyfried, W.E., Seewald, J.S., Berndt, M.E., Ding, K., Foustoukos, D.I., 2003. Chemistry of hydrothermal vent fluids from the Main Endeavour Field, northern Juan de Fuca Ridge: Geochemical controls in the aftermath of June 1999 seismic events. *Journal of Geophysical Research-Solid Earth* 108.
- Shikazono, N., 1994. Precipitation mechanisms of barite in sulfate-sulfide deposits in back-arc basins. *Geochimica et Cosmochimica Acta* 58, 2203-2213.
- Shikazono, N., Kawabe, H., Ogawa, Y., 2012. Interpretation of Mineral Zoning in Submarine Hydrothermal Ore Deposits in Terms of Coupled Fluid Flow-Precipitation Kinetics Model. *Resource Geology* 62, 352-368.
- Teagle, D.A.H., Alt, J.C., Chiba, H., Humphris, S.E., Halliday, A.N., 1998. Strontium and oxygen isotopic constraints on fluid mixing, alteration and mineralization in the TAG hydrothermal deposit. *Chemical Geology* 149, 1-24.
- Tivey, M.K., 1995. The influence of hydrothermal fluid composition and advection rates on black smoker chimney mineralogy - insights from modeling transport and reaction. *Geochimica Et Cosmochimica Acta* 59, 1933-1949.
- Tivey, M.K., 2004. Environmental conditions within active seafloor vent structures: sensitivity to vent fluid composition and fluid flow, in: Wilcock, W., Cary, C., DeLong, E., Kelley, D., Baross, J. (Eds.), *Subseafloor Biosphere at Mid-Ocean Ridges*, Geophysical Monograph Series, No. 144. American Geophysical Union, Washington, DC, pp. 137-152.
- Tivey, M.K., Delaney, J.R., 1986. Growth of large sulfide structures on the Endeavour Segment of the Juan-de-Fuca Ridge. *Earth and Planetary Science Letters* 77, 303-317.
- Tivey, M.K., McDuff, R.E., 1990. Mineral precipitation in the walls of black smoker chimneys - a quantitative model of transport and chemical-reaction. *Journal of Geophysical Research-Solid Earth and Planets* 95, 12617-12637.
- Tivey, M.K., Olson, L.O., Miller, V.W., Light, R.D., 1990. Temperature-measurements during initiation and growth of a black smoker chimney. *Nature* 346, 51-54.
- Tivey, M.K., Stakes, D.S., Cook, T.L., Hannington, M.D., Petersen, S., 1999. A model for growth of steep-sided vent structures on the Endeavour Segment of the Juan de Fuca Ridge: Results of a petrologic and geochemical study. *Journal of Geophysical Research-Solid Earth* 104, 22859-22883.
- Turcotte, D., 1997. *Fractals and Chaos in Geology and Geophysics*, Cornell University, New York.
- Turekian, K.K., 1968. *Oceans*. Prentice-Hall, Englewood Cliffs, N.J.
- Ulrich, M., Bodnar, R., 1988. Systematics of stretching of fluid inclusions; II, Barite at 1 atm confining pressure. *Economic Geology* 83, 1037-1046.
- Vearncombe, S., Barley, M.E., Groves, D.I., McNaughton, N.J., Mikucki, E.J., Vearncombe, J.R., 1995. 3.26 Ga Black smoker-type mineralization in the Strelley Belt, Pilbara-Craton, Western-Australia. *Journal of the Geological Society* 152, 587-590.

- Von Damm, K.L., 1990. Seafloor hydrothermal activity - black smoker chemistry and chimneys. *Annual Review of Earth and Planetary Sciences* 18, 173-204.
- Widanagamage, I.H., Schauble, E.A., Scher, H.D., Griffith, E.M., 2014. Stable strontium isotope fractionation in synthetic barite. *Geochimica Et Cosmochimica Acta* 147, 58-75.
- Wolery, T.J., 1992. EQ3NR, A Computer Program for Geochemical Aqueous Speciation-Solubility Calculations: Theoretical Manual, User's Guide, and Related Documentation (Version 7.0), Lawrence Livermore Natl. Lab, Livermore, California.
- Wolery, T.J., Daveler, S.A., 1992. EQ6, A Computer Program for Reaction Path Modeling of Aqueous Geochemical Systems: Theoretical Manual, User's Guide, and Related Documentation (Version 7.0), Lawrence Livermore Natl. Lab, Livermore, California.
- Yao, H.-Q., Zhou, H.-Y., Peng, X.-T., Bao, S.-X., Wu, Z.-J., Li, J.-T., Sun, Z.-L., Chen, Z.-Q., Li, J.-W., Chen, G.-Q., 2009. Metal sources of black smoker chimneys, Endeavour Segment, Juan de Fuca Ridge: Pb isotope constraints. *Applied Geochemistry* 24, 1971-1977.
- You, C.F., Butterfield, D.A., Spivack, A.J., Gieskes, J.M., Gamo, T., Campbell, A.J., 1994. Boron and halide systematics in submarine hydrothermal systems - effects of phase-separation and sedimentary contributions. *Earth and Planetary Science Letters* 123, 227-238.

Tables

Table 1: Fluid compositions used in mixing calculations

	Endeavour Vent Fluid ¹	Seawater ²
Temperature (°C)	350	2
pH (25°C)	4.2	8
Mg mmol/kg	0	53.2
Cl mmol/kg	425	550
Na mmol/kg	320	460
Ca mmol/kg	32.7	10.3
K mmol/kg	24.4	10.2
SiO ₂ mmol/kg	15.7	0.1
Fe mmol/kg	915	0
Mn mmol/kg	289	0
Ba mmol/kg	31	0.1
Sr mmol/kg	134	87
SO ₄ mmol/kg	0	28.3
H ₂ S mmol/kg	5.4	0
CO ₂ mmol/kg	12.6	2.5
H ₂ umol/kg	42	Log fO ₂ = -0.759
NH ₃ umol/kg	500	4
⁸⁷ Sr/ ⁸⁶ Sr	0.7034 ³	0.7092 ⁴

¹ Endeavour vent fluid chemistry is from the Grotto vent (Butterfield et al., 1994) with Ba from Seyfried et al. (2003), H₂ from Lilley et al. (1993), NH₃ of 500 as an approximate value.

² Seawater values from Butterfield et al. (1994), Seyfried et al. (2003) and Tivey (2004).

³ This study (see text)

⁴ From Butterfield et al. (2001)

Table 2: Major element concentrations in barite from ALV2467-R2 (errors given in 2RSD %).
Locations correspond to laser ablation tracks in Figure 5C.

	Ba (ppm)	Sr (ppm)	Ca (ppm)	K (ppm)
Line A	583466 ± 7%	17140 ± 10%	4975 ± 13%	230 ± 15%
Line B	567340 ± 7%	22086 ± 7%	8933 ± 5%	352 ± 8%
Line C	561626 ± 7%	13380 ± 7%	4221 ± 7%	140 ± 10%
Line D	563516 ± 8%	22731 ± 8%	8176 ± 7%	286 ± 9%
Line E	588013 ± 8%	25708 ± 9%	11367 ± 5%	419 ± 8%
Line F	558996 ± 9%	14176 ± 9%	4517 ± 8%	156 ± 13%
Line G	574019 ± 8%	7403 ± 8%	1912 ± 8%	41 ± 22%
Line H	612912 ± 7%	11439 ± 11%	3528 ± 13%	101 ± 20%

Table 3: Bulk $^{87}\text{Sr}/^{86}\text{Sr}$, calculated fluid mixing and fluid mixture temperatures for hydrothermal chimneys samples.

Sample	Barite crystal habit	Vent Field	$^{87}\text{Sr}/^{86}\text{Sr} \pm 2\sigma$	% Hydrothermal fluid ¹	Temperature of fluid mixture (°C) ²	[Sr]/[Ba] (Whole Rock) ³	[Sr]/[Ba] (Fluid) ⁴	Apparent K_D ⁵
ALV1452-1A	Dendritic	Main Endeavour	0.707581 ± 0.000011	17	61	0.069	2.62	0.004
ALV4446-1628	Acicular/bladed	Main Endeavour	0.706058 ± 0.000009	39	136	0.050	2.53	0.006
ALV3589-R2	Small tabular	Main Endeavour	0.705635 ± 0.000010	46	162	0.051	2.52	0.007
ALV4450-1829	Acicular/bladed	Mothra	0.705461 ± 0.000009	49	173	0.045	2.52	0.007
ALV2072-7	Acicular	Main Endeavour	0.705116 ± 0.000010	56	196	0.063	2.51	0.010
ALV2467-R3	Acicular/bladed	Clam Bed	0.704816 ± 0.000011	62	218	0.008	2.50	0.001
ALV2068-1	Acicular/bladed	Main Endeavour	0.704779 ± 0.000010	63	221	0.056	2.50	0.010
ALV2461-R6-4	Acicular	High Rise	0.704630 ± 0.000010	66	233	0.025	2.50	0.004
ALV2464-R4	Tabular	High Rise	0.704584 ± 0.000009	67	237		2.50	
ALV3000C	Acicular	Salty Dawg	0.704545 ± 0.000009	68	240	0.021	2.50	0.004
ALV2415-1D(3)	Acicular	Main Endeavour	0.704525 ± 0.000010	69	242	0.048	2.50	0.009
ALV1452-2	Acicular	Main Endeavour	0.704496 ± 0.000007	70	244	0.046	2.50	0.008
ALV2449-1	Acicular	Main Endeavour	0.704380 ± 0.000010	72	254	0.018	2.50	0.003
TiveyMisc2	Small tabular	Main Endeavour	0.704198 ± 0.000012	77	270	0.022	2.50	0.004
ALV2467-R9	Tabular	North of Clam Bed	0.703862 ± 0.000011	86	301	0.026	2.49	0.005
ALV2467-R2	Tabular	North of Main Endeavour	0.703798 ± 0.000009	88	308	0.020	2.49	0.004

¹ % relative contribution calculated using equation (2).

² Temperatures are calculated using equation (3).

³ Ratio determined using whole rock Sr and Ba concentrations (see Supplementary Table S1).

⁴ Calculated based on the degree of mixing (using $^{87}\text{Sr}/^{86}\text{Sr}$) between endmember seawater and hydrothermal fluids (see Table 1 for details).

⁵ $D_{\text{Sr}} = ([\text{Sr}]/[\text{Ba}]_{\text{Whole Rock}})/([\text{Sr}]/[\text{Ba}]_{\text{Fluid}})$

Table 4: Laser ablation strontium isotope ratios ($^{87}\text{Sr}/^{86}\text{Sr}$) across single barite crystals from samples ALV2464-R4 and ALV2467-R2.

Analysis ¹	$^{87}\text{Sr}/^{86}\text{Sr} \pm 2\sigma$	Relative Sr intensity ² $\pm 2\sigma$	% Hydrothermal Fluid ³	Temperature ⁴ (°C)
ALV2464-R4				
1	0.70447 \pm 0.00022	4.73 \pm 0.14	70	246
2	0.70468 \pm 0.00026	3.36 \pm 0.11	65	229
3	0.70434 \pm 0.00029	4.27 \pm 0.15	73	257
4	0.70456 \pm 0.00029	4.60 \pm 0.16	68	239
5	0.70442 \pm 0.00026	4.74 \pm 0.12	71	250
6	0.70453 \pm 0.00024	3.67 \pm 0.02	69	241
7	0.70447 \pm 0.00027	5.55 \pm 0.05	70	246
8	0.70438 \pm 0.00024	3.23 \pm 0.03	72	253
9	0.70449 \pm 0.00020	2.60 \pm 0.01	70	245
10	0.70413 \pm 0.00020	4.71 \pm 0.02	79	275
11	0.70439 \pm 0.00026	5.07 \pm 0.04	72	253
12	0.70431 \pm 0.00027	5.42 \pm 0.06	74	260
13	0.70445 \pm 0.00027	6.75 \pm 0.04	71	248
14	0.70442 \pm 0.00025	5.81 \pm 0.05	71	250
15	0.70428 \pm 0.00025	4.06 \pm 0.03	75	263
16	0.70485 \pm 0.00022	3.09 \pm 0.04	62	216
17	0.70421 \pm 0.00023	4.44 \pm 0.04	77	268
18	0.70436 \pm 0.00025	7.83 \pm 0.03	73	255
19	0.70436 \pm 0.00021	8.14 \pm 0.12	73	256
20	0.70463 \pm 0.00025	2.62 \pm 0.12	66	233
21	0.70509 \pm 0.00025	1.34 \pm 0.04	56	198
ALV2467-R2				
1	0.70394 \pm 0.00021	4.22 \pm 0.05	84	294
2	0.70373 \pm 0.00018	5.80 \pm 0.04	90	314
3	0.70401 \pm 0.00019	4.04 \pm 0.01	82	287
4	0.70392 \pm 0.00022	6.04 \pm 0.01	84	295
5	0.70435 \pm 0.00025	1.91 \pm 0.03	73	257

¹ Analysis numbers correspond to locations shown on Fig. 5D

² Relative Sr intensity, measured during laser ablation analysis can be used as a proxy for Sr-concentration within the barite crystal

³ % hydrothermal fluid is calculated using equation (2)

⁴ Temperature is calculated using equation (3)

Table 5: Calculated fluid salinities from fluid inclusions

Inclusion #	Final Melting Temperature (T _m , °C)	Salinity (wt. %) ¹
ALV2464-R4 (Barite)		
1	-5.1	8.0
2	-3.8	6.2
3	-5.1	8.0
4	-5.3	8.3
5	-5.4	8.4
6	-4.6	7.3
7	-5.6	8.7
8	-3.5	5.7
ALV2467-R2 (Barite)		
1	-3.5	5.7
2	-4.7	7.4
ALV2464-R4 (Amorph. Silica)		
1	-2.0	3.4

¹ Calculated using equation 1

Table 6: Partition coefficients for individual growth zones within a single barite crystal from ALV 2467-R2.

Analyzed Pair ¹	Sr/Ba (fluid) ²	Sr/Ba (barite) ³	Apparent K _D ⁴
2 - B	5.09	0.04	0.008
3 - C	5.09	0.02	0.005
4 - D	5.09	0.04	0.008
5 - F	5.21	0.03	0.005

¹ Number/letter combinations refer to paired analyses from single growth zones in Fig. 5C.

² Calculated using predicted fluid chemistry based on degree of mixing (determined by ⁸⁷Sr/⁸⁶Sr) and endmember fluid properties (Table 1).

³ Calculated using data in Table 2.

⁴ $K_D = ([Sr]/[Ba])_{\text{Barite}} / ([Sr]/[Ba])_{\text{Fluid}}$

Figures

Figure 1:

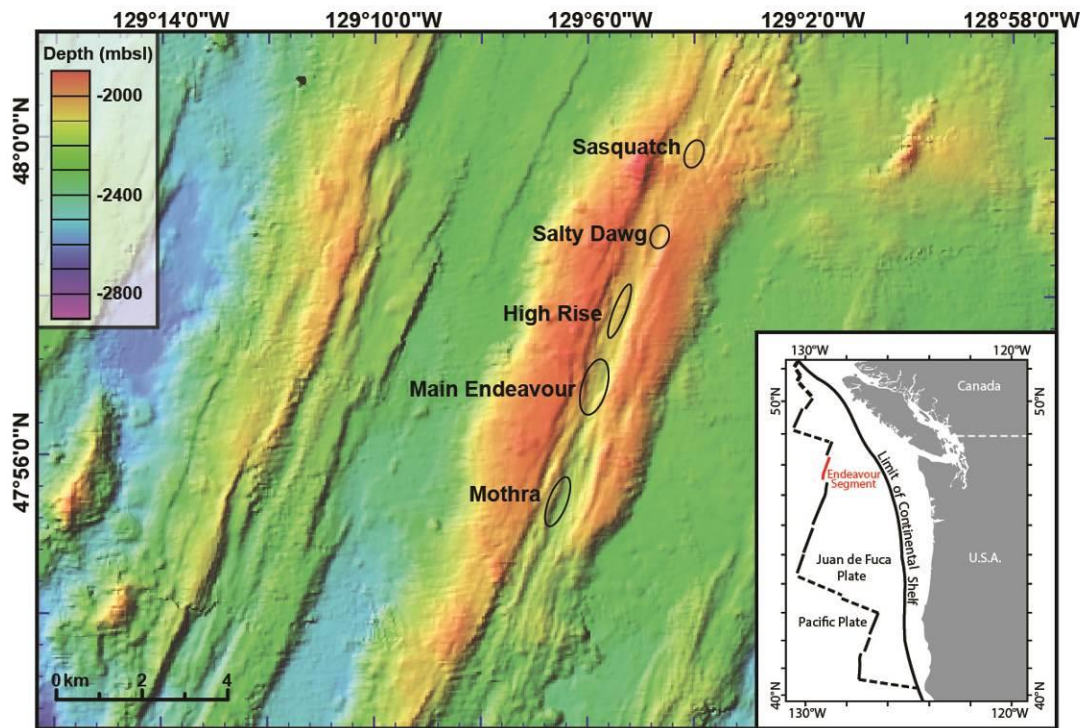


Figure 1: Bathymetric map of the Endeavour Segment, with the locations of the major active vent fields. Inset map shows the location of the Endeavour Segment on the Juan de Fuca Ridge. Bathymetric data collected using hull-mounted EM300 multibeam system on the *R/V Thomas G. Thompson* (TN146) (Kelley, 2002; www.geomapapp.org)

Figure 2:

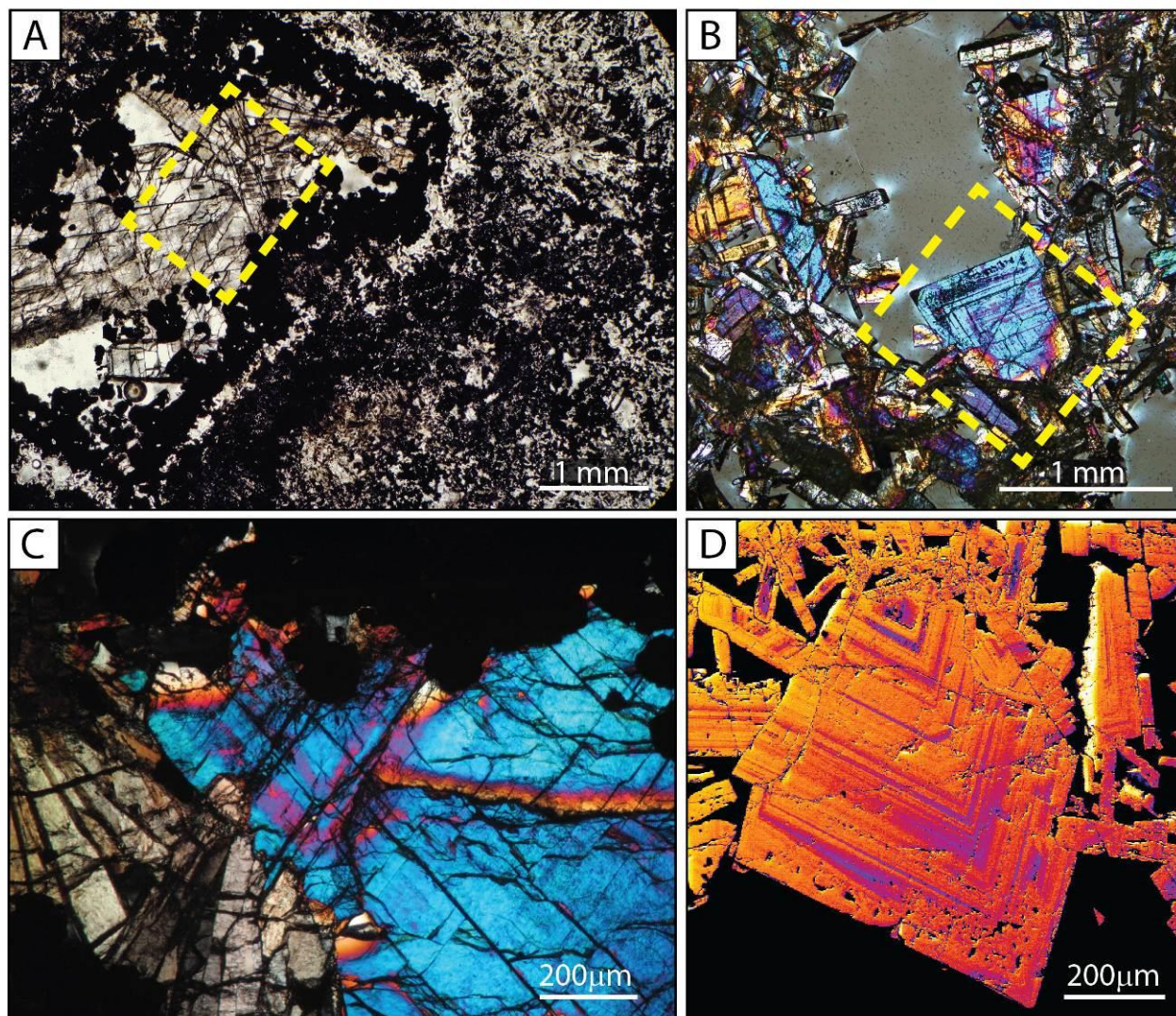


Figure 2: A: Plane-polarized photomicrograph of ALV2467-R2, with a fluid conduit infilled by tabular barite. The conduit is lined with dark-red to opaque rounded sphalerite grains. The surrounding matrix consists of bladed barite, fine sphalerite with minor pyrite and late-stage amorphous silica. B: Cross-polarized photomicrograph of ALV2464-R4, showing tabular and bladed barite crystals that grew into open pore space. Yellow dashed boxes in A and B show location of detailed images in C and D, respectively. C: Cross-polarized photomicrograph of tabular barite crystal from A. The magenta colour within the blue crystal indicates Sr-rich growth zones. D: Coloured electron microprobe backscatter image of barite crystal from B. Again, magenta colours indicate Sr-rich growth zones. Some interference colours of barite in cross-polarized images in this figure, as well as Figure 3, appear as second-order colours due to the thin sections have a thickness of slightly greater than 30 μm .

Figure 3:

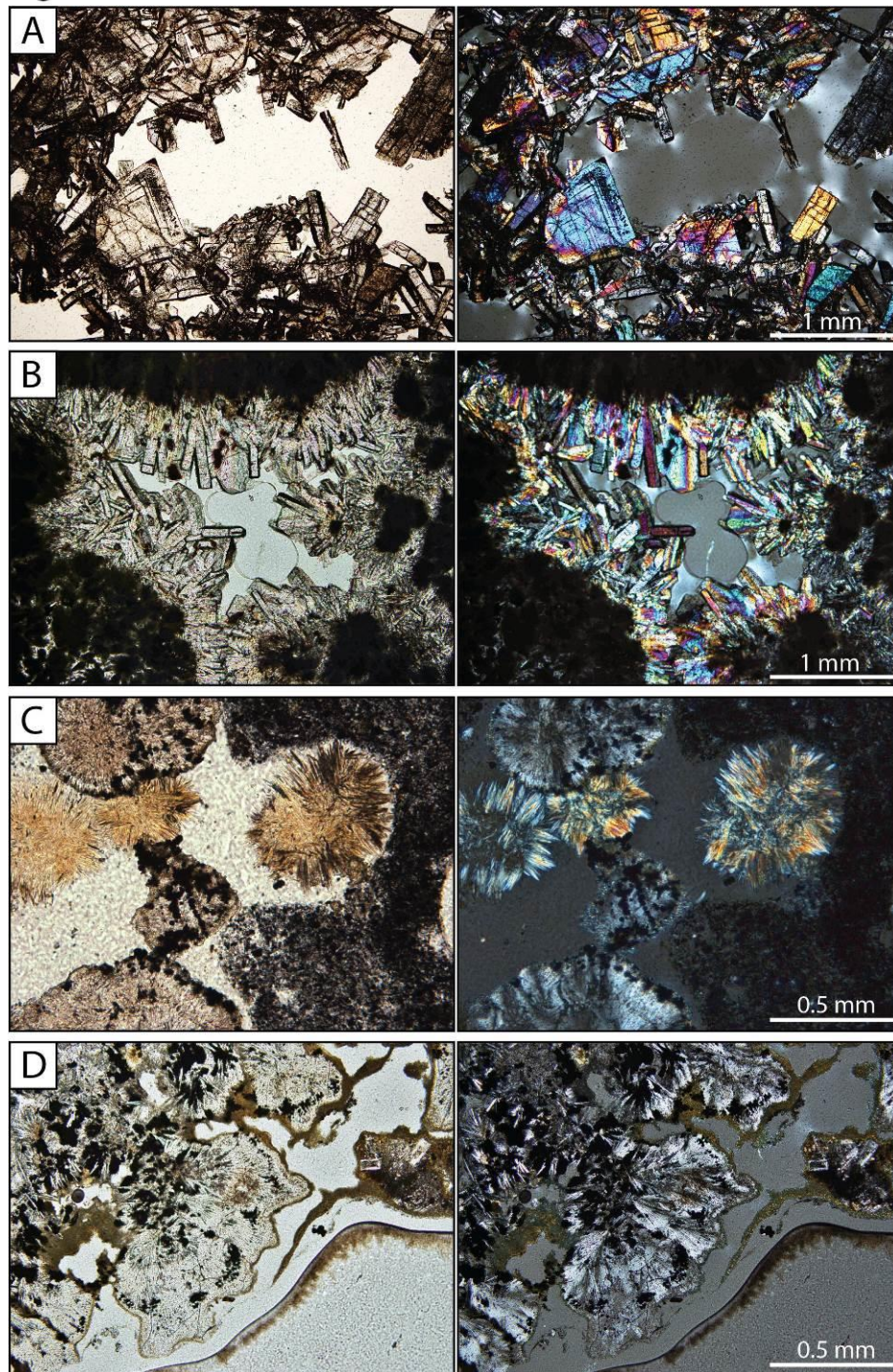


Figure 3: Transmitted light photomicrographs (plane-polarized in left column, cross-polarized in right column) showing the range of crystal morphologies for barite crystals within hydrothermal vents from the Endeavour Segment. A: Euhedral tabular and bladed crystals; B: bladed crystals; C: radiating acicular crystals; and D: acicular and dendritic crystals.

Figure 4:

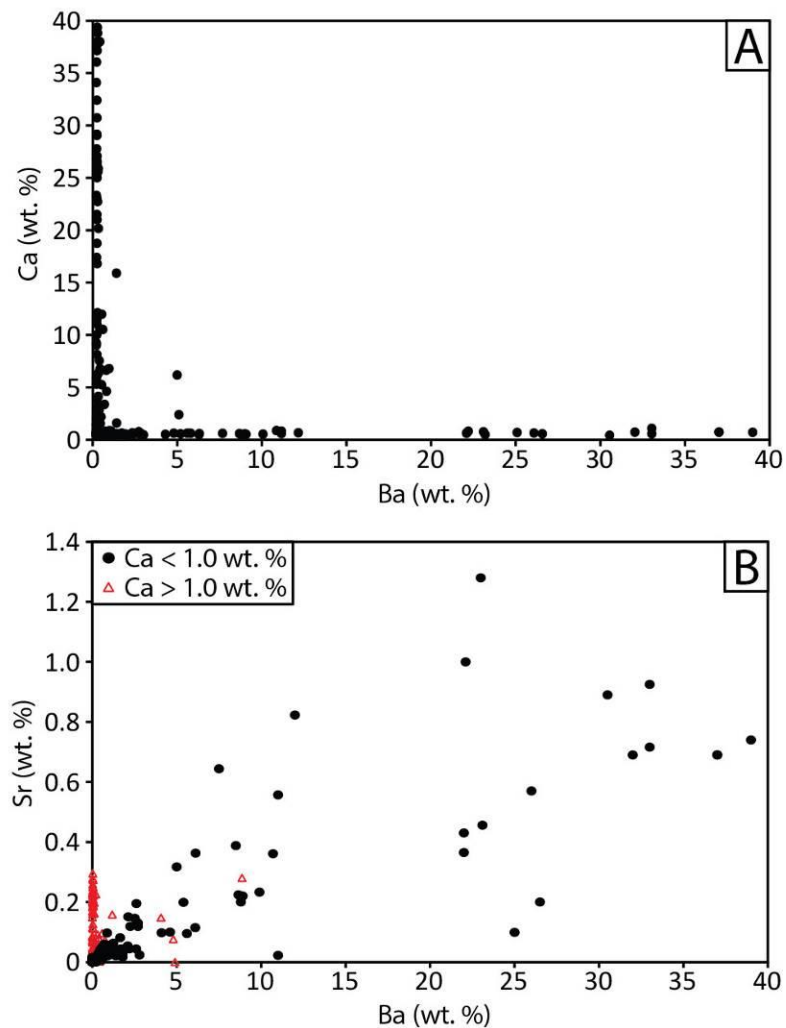


Figure 4: A: Plot of whole rock Ca vs. Ba for 335 chimney samples from all major vent fields and inactive vent sites within the axial valley showing a distinct negative correlation, with Ba-rich samples having low Ca concentrations, and Ca-rich samples having low Ba concentrations. Samples B: Strontium concentration plotted against Ba concentration. Samples are grouped as either Ca-rich (red triangles) or Ca-poor (black circles). Because Sr partitions predominantly into anhydrite or barite, the low concentrations of Ca in the Ba-rich samples indicates that barite is the primary host for Sr in these samples, and whole rock Sr/Ba values are representative of the Sr/Ba content within the barite.

Figure 5:

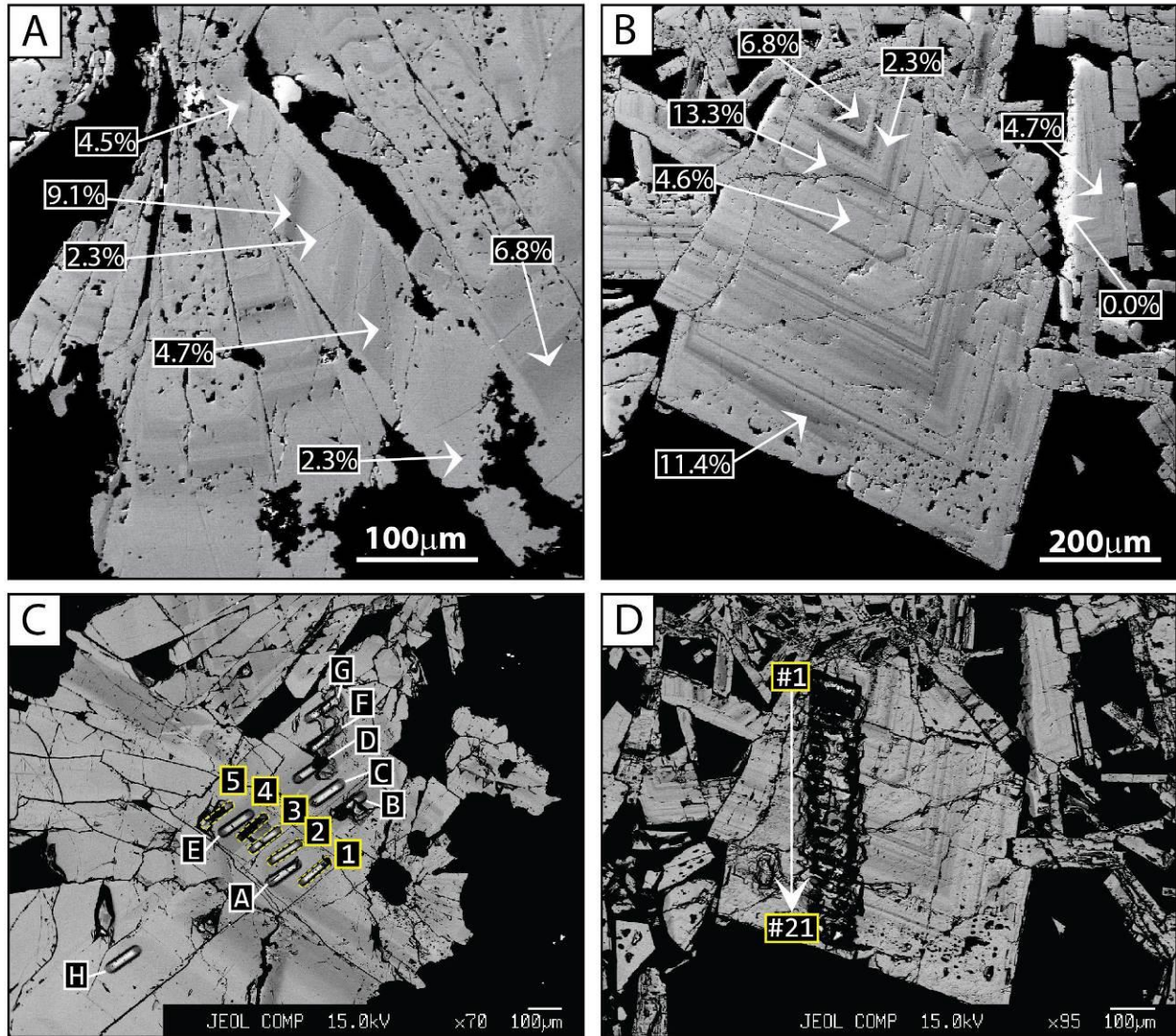


Figure 5: Electron microprobe backscatter images of barite crystals from samples ALV2467-R2 (A and C) and ALV2464-R4 (B and D) showing Sr-rich (dark) and Sr-poor (light) growth zones. Numbers in A and B refer to the percent Sr occupying the cation site within barite, normalized to 100% Ba+Sr+Ca. Panels C and D show locations of laser ablation analyses. Lines A-H in C represent locations of elemental analyses summarized in Table 2. Lines 1-5 (C, outlined in yellow) and the closely-spaced parallel lines 1-21 (D) are locations of $^{87}\text{Sr}/^{86}\text{Sr}$ analyses, summarized in Table 4.

Figure 6:

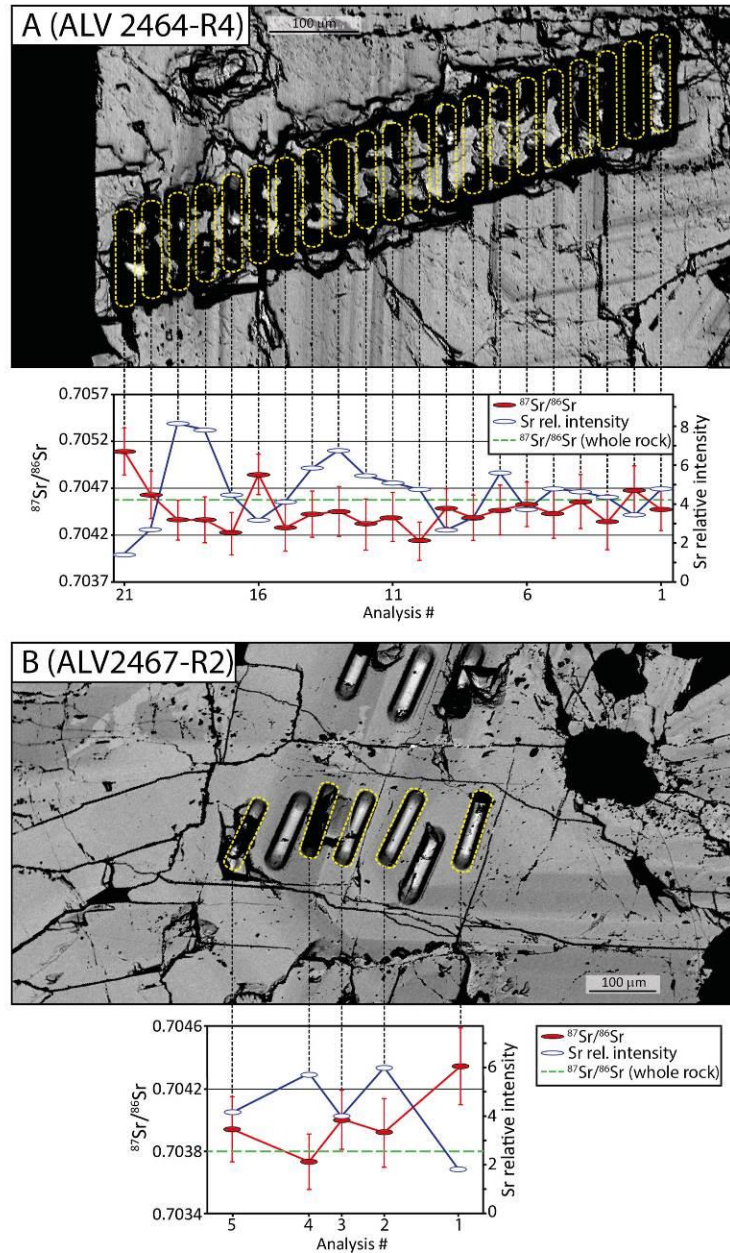


Figure 6: Results of $^{87}\text{Sr}/^{86}\text{Sr}$ variability and Sr-concentrations within single barite crystals from ALV2464-R4 (A) and ALV2467-R2 (B). The locations of the laser raster for each analysis are outlined on the associated backscatter. For ALV2467-R2, the rasters not outlined in yellow are from elemental analyses indicated in Fig. 5C. The relationship between Sr concentration and zonation within the crystals can be clearly seen, with darker regions having a higher Sr/Ba. The width of each data point on the plots is equal to the width of each ablation line (25 μm). Uncertainties for relative Sr concentrations are smaller than the symbols.

Figure 7:

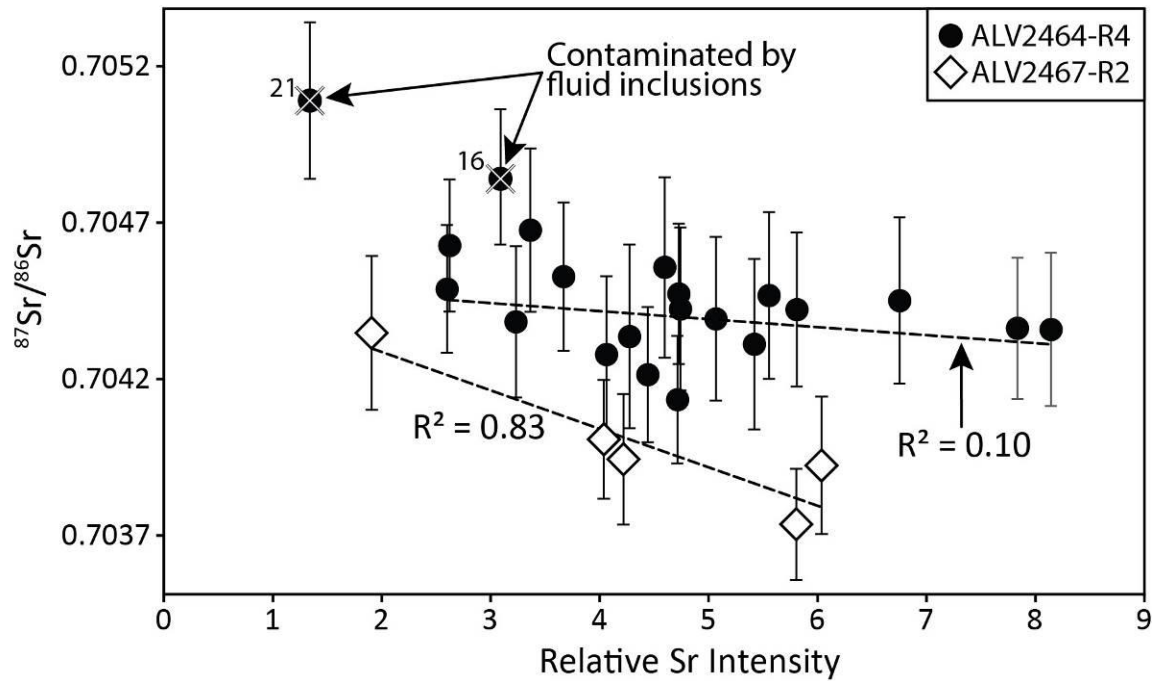


Figure 7: Plot of $^{87}\text{Sr}/^{86}\text{Sr}$ versus the relative intensity of Sr (a proxy for Sr-concentration based on the relative strength of the Sr signal from the mass spectrometer) for samples ALV2464-R4 and ALV2467-R2. For ALV2464-R4 (black circles), there is very little variation in Sr-isotope composition with concentration within the crystal. Analyses 16 and 21 were ignored when plotting the regression line, as these samples were contaminated by large fluid inclusions. For ALV2467-R2 (open diamonds), a slight negative correlation is present, indicating a decreasing contribution of seawater (lower $^{87}\text{Sr}/^{86}\text{Sr}$) with higher Sr/Ba in the crystal.

Figure 8:

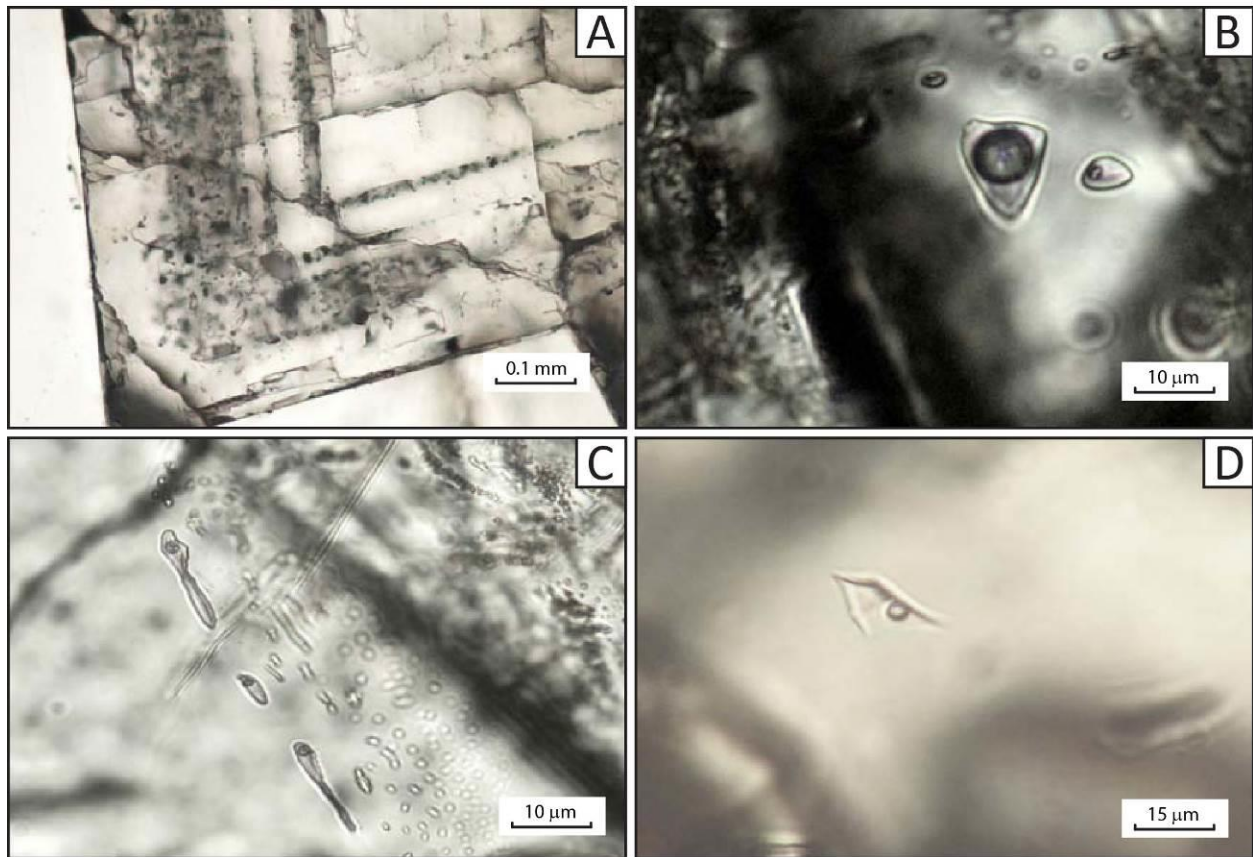


Figure 8: Occurrence of aqueous fluid inclusions in barite and amorphous silica. A) Tabular, zoned barite crystal comprising several growth zones delineated by primary fluid and solid inclusions. B) Primary fluid inclusions in barite with variable vapor/liquid ratios. C) Late secondary ("immature") inclusions in barite. D) Inclusions in amorphous silica.

Figure 9:

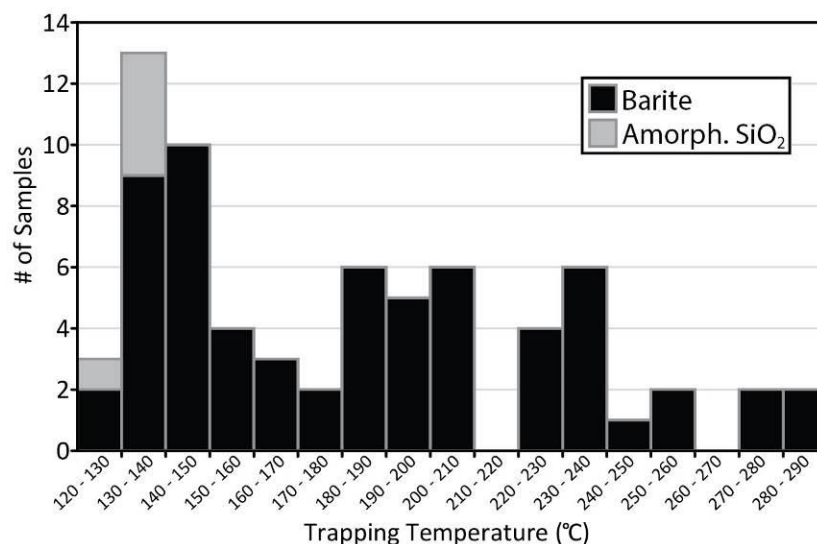


Figure 9: Histogram of pressure-corrected fluid inclusion formation temperatures for barite and amorphous silica. The majority of primary inclusions from well-formed barite crystals indicate formation temperatures of between 180 and 240°C. Secondary barite inclusions and inclusions within amorphous silica formed at lower temperatures (130 to 170°C). Only the smallest, smooth-walled workable inclusions were used, and care was taken during the homogenization measurements, observing continuously during heating, to avoid possible overheating and stretching of the inclusions. However, the large range of homogenization temperatures may reflect an increase in volume upon heating.

Figure 10:

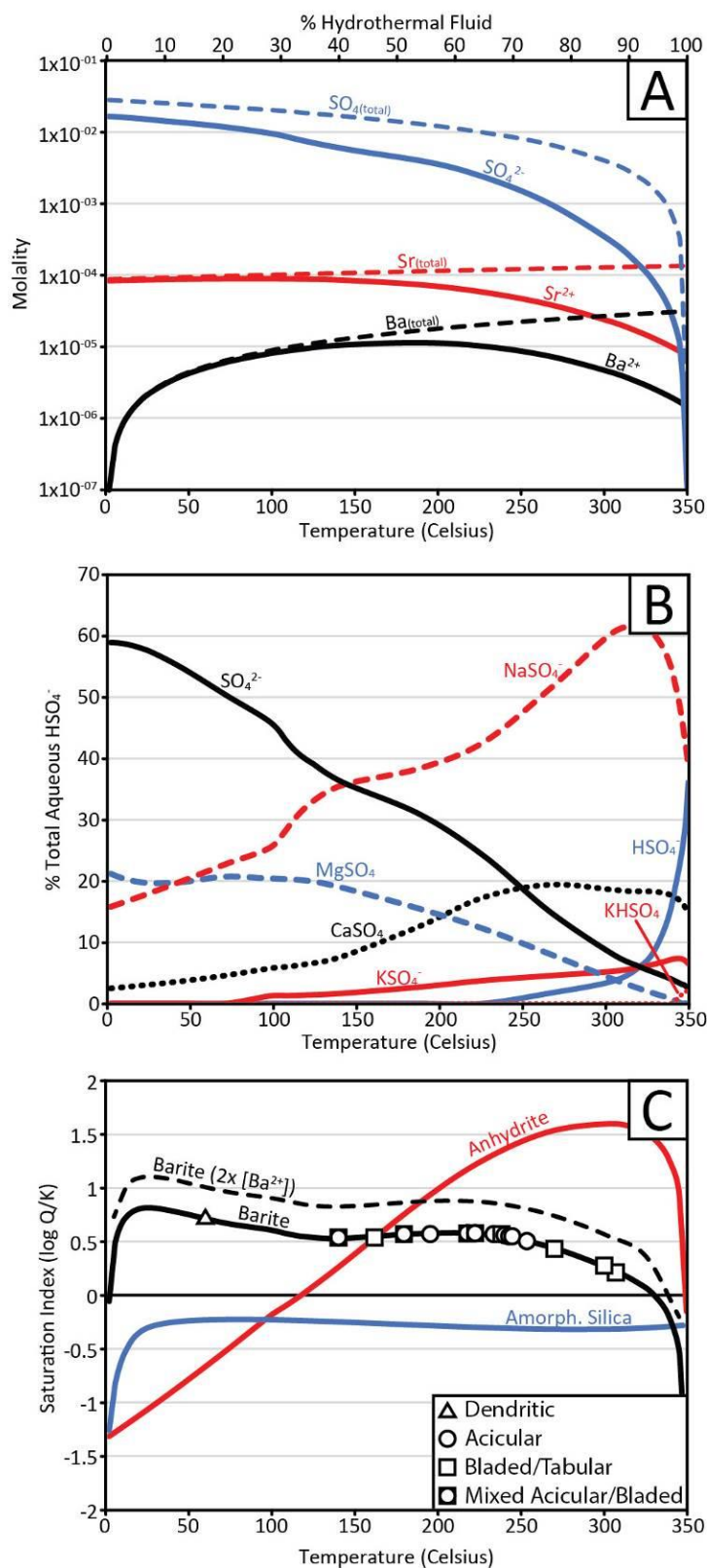


Figure 10: Results of chemical modelling of fluid mixing. A: Changes in free and total Ba^{2+} , Sr^{2+} and SO_4^{2-} concentrations as a function of both temperature and degree of mixing. B: Variation in the relative proportions of different SO_4^{2-} -bearing species at different mixing temperatures. C: Degree of super- or under-saturation of barite, anhydrite and amorphous silica as a function of fluid mixing temperature. Mineral precipitation occurs at saturation indices greater than zero. Samples are plotted based on mixing temperatures determined using barite $^{87}\text{Sr}/^{86}\text{Sr}$ values. Higher degrees of supersaturation result in formation of dendritic, as opposed to well-formed, barite.

Figure 11:

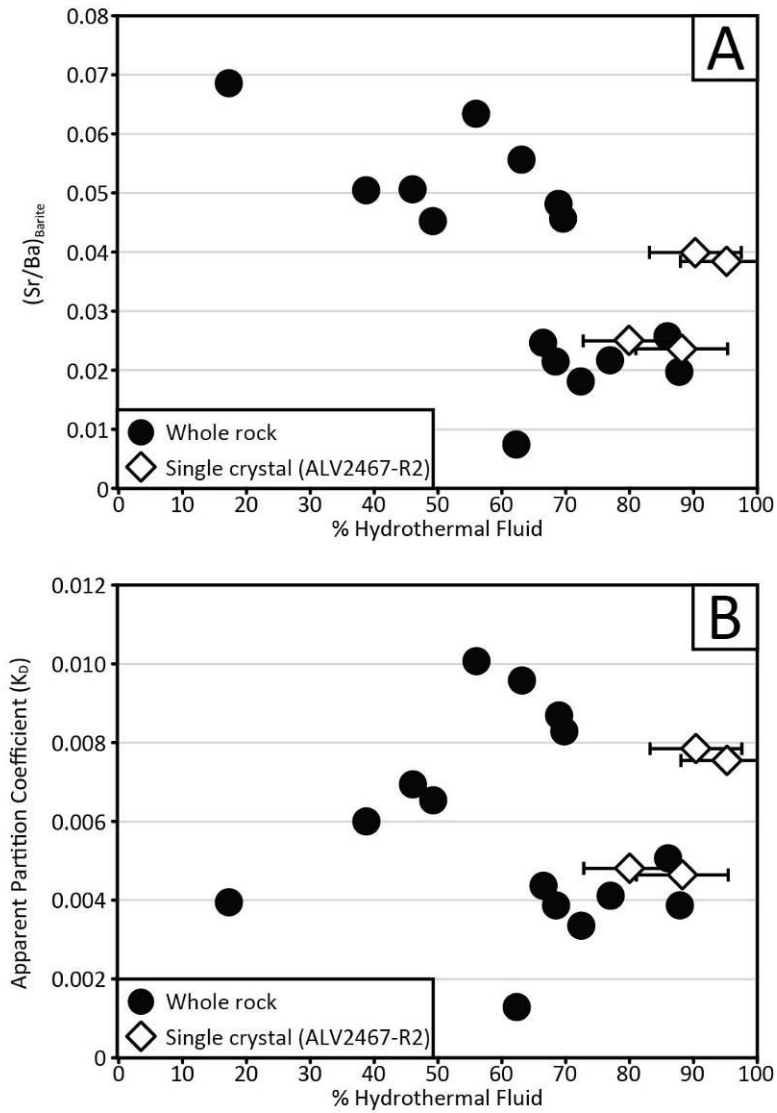


Figure 11: Whole rock and single crystal Sr/Ba (A) and apparent partition coefficients (B) plotted against mixing temperature, showing a general decrease in Sr substitution at higher formation temperatures. Open diamonds represent Sr/Ba from different zones within a single euhedral barite crystal (Fig. 6B) and indicate variable Sr substitution over small changes in temperature. Whole rock temperature uncertainties are smaller than the symbol size, plotted temperature uncertainties for ALV2467-R2 are 2σ .